The Static Quark Potential at Finite Temperature and Density

Kenneth Granahan B.S.c

The Static Quark Potential at Finite Temperature and Density

Kenneth Granahan B.S.c

This Thesis is presented for the degree of Masters by Research

to the University of Maynooth,

Department of Theoretical Physics

October 2018

Department Head:

Dr. Jon-Ivar Skullerud

Research Advisor:

Dr. Jon-Ivar Skullerud

Contents

1 Abstract **5**

2 Introduction **5**

3 Lattice QCD **7**

3.1 Euclidean Space 7

3.2 Discretizing Spacetime 10

3.3 Gauge Fields on the lattice 11

3.4 Fermions on the lattice 12

3.5 Lattice Actions 13

3.6 Monte Carlo Methods 15

3.7 Lattice QCD at $T \neq 0$. 16

3.8 $\mu \neq 0$. The sign problem 17

4 Definition of the static quark potential **19**

4.1 The Thermal Wilsonloop 19

4.2 Spectral Functions 21

4.3 Bayesian Inference 23

5 Details of the Numerical Simulations and Results **25**

5.1 High Temperature Analysis 25

5.1.1 Simulation parameters 25

5.1.2 Results 27

5.2 Two Colour High Density Analysis 40

5.2.1 Simulation parameters 40

6 Conclusions **50**

A Lattice QCD **50**

A.1 γ_E^μ algebra 50

A.2 Gauge transformation of $U(x, y)$ 52

A.3 Calculus with Grassmann variables 53

A.3.1 Differentiation of Grassmann variables 54
A.3.2 Integration of Grassmann variables 55
A.4 Continuum limit of the Wilson Gauge Action 56
A.5 Continuum limit of the Wilson Fermion Action 59
A.6 Integration of the fermionic fields 61
A.7 $\det(M)$ is real for $\mu = 0$ and complex for $\mu \neq 0$ 62
A.8 $\det(M(\mu))$ is real in 2 colour QCD 63
A.9 Thermal correlators 64

1 Abstract

We present calculations of the potential energy between an infinitely heavy quark-antiquark pair at high temperatures and densities. The calculations are carried out via lattice QCD in conjunction with a recently developed Bayesian inference method. We provide a detailed overview lattice QCD, Bayesian inference methods and the potential energy itself. We conclude by considering some suitable potential models put forth in the literature. At sufficiently high temperature we observe the apparent onset of deconfinement, while at high densities no such deconfinement is observed.

2 Introduction

The physics of strong interactions has proved to be a complex and phenomenological rich field of study. The existence of different quark flavors, as well as the non-abelian nature of their interactions, gives rise to a diverse range of physical systems, which may be described by quantum chromodynamics (QCD). This non-abelian property of strong interactions also presents many challenges, in particular, it suffers from both ultraviolet and infrared divergences, which greatly reduces the viability of perturbative descriptions. Indeed, this proved such a hindrance, that it required a new formulation of the underlying theory, lattice QCD, which provides non-perturbative calculations of observables.

Despite the non-perturbative framework lattice QCD offers, strong interactions retain quite complicated descriptions, causing many to seek systems where these descriptions may be greatly simplified. One such system which is relevant to this thesis, is the dynamics of charm and bottom mesons (hereafter we will denote these as $Q\overline{Q}$ bound states). The large mass of these quark flavors ($m_c = 1.275 \pm 0.025$GeV, $m_b = 4.18 \pm 0.03$GeV [20]) has been thought to leave non-relativistic descriptions as a viable option to describe $Q\overline{Q}$ bound states. With this motivation, calculations of the potential energy between a heavy quark anti-quark pair (which we shall refer to as the static quark potential) have been carried out. Such descriptions have useful applications in areas such as heavy ion-collisions and neutron star formation. One particularly noteworthy application is the study of the Quark-Gluon Plasma (QGP)[19], which is a state of matter thought to exist at sufficiently high temperature. The dynamics of the $Q\overline{Q}$ bound state is believed to serve as a useful probe into the properties of hot matter created in heavy-ion collisions [4].

The calculation of the static quark potential has been found to be more involved than first thought. Originally the potential was calculated by applying an exponential fit to the ground state energy of the $Q\overline{Q}$ bound state [7]. Later work carried out by M.Laine et al [18] showed that at non-zero temperature, such a potential becomes complex with a leading order imaginary component

proportional to the temperature T, rendering exponential fits unusable for high temperature descriptions.

It took the development of Effective Fields Theories (EFT) which exploits the hierarchy of scales present in QCD ($m_Q \gg m_Q v \gg m_Q v^2$, where m_Q is the heavy quark mass and v is its velocity), to provide a more rigorous approach to such calculations. This EFT treatment relies on a procedure known as matching, in which a suitable correlator is computed in the EFT, then equated to an appropriately chosen correlator in QCD. This approach has produced reassuring results, such as a coulomb term up to leading order in the potential and offers a natural framework to study spin dependent potential models [6]. However, at finite temperature T this EFT approach is hindered by the use of perturbative expansions in T and Debye mass m_D (see [5]), which only leaves it as a viable description for particular temperature ranges (e.g. $m_Q v \ll gT \ll m_Q$, where g is the gauge coupling).

In this thesis we will be calculating this complex potential using a relatively recent procedure outlined in [23], which makes use of the spectral function representation of the colour singlet correlator to infer numerically, the real and imaginary parts of the static quark potential. This methodology is useful in that it valid at any temperature, provided the numerical data has sufficiently high accuracy. Here we provide a thorough description of the underlying theory and present calculations of the complex static quark potential at both high temperature and high density using this spectral function representation.

3 Lattice QCD

Lattice QCD is a non-perturbative formulation of QCD in which we approximate Minkowski space as a discrete set of lattice points. We then place some action on this lattice whose continuum limit converges to the QCD action. Recall that the QCD action is:

$$S_{QCD} = \int d^4x \, \mathrm{tr} \left\{ G^{\mu\nu} G_{\mu\nu} \right\} + \sum_f \overline{\psi}_f \left(i\gamma^\mu D_\mu - m_f \right) \psi_f, \tag{1}$$

where

$$G^{\mu\nu} = F^{\mu\nu} + ig \left[A_\mu, A_\nu \right], \tag{2}$$
$$F^{\mu\nu} = \partial^\mu A^\nu - \partial^\nu A^\mu, \tag{3}$$
$$D_\mu = \partial_\mu - igA_\mu, \tag{4}$$
$$A_\mu = A_\mu^a T^a \tag{5}$$
$$\{\gamma^\mu, \gamma^\nu\} = 2g^{\mu\nu}, \tag{6}$$
$$\overline{\psi} = \psi^\dagger \gamma^0, \tag{7}$$

where T^a are the generators of $SU(N)$ in the adjoint representation. In the above expression we are summing over all quark flavors f and the trace $\mathrm{tr} \left\{ G^{\mu\nu} G_{\mu\nu} \right\}$ is taken over the colour indices.

We make use of the path integral formulation to calculate the expectation value of an operator O via the equation:

$$\langle O \rangle = \frac{1}{Z} \int DA_\mu D\overline{\psi} D\psi \exp \left[-iS_{QCD} \right] O. \tag{8}$$
$$\text{where } Z = \int DA_\mu D\overline{\psi} D\psi \exp \left[-iS_{QCD} \right]. \tag{9}$$

We need only determine which action to use as well as how our fields and measures $DA_\mu, D\overline{\psi}, D\psi$ appear on the lattice.

In this section we briefly discuss how the lattice formulation of QCD is carried out at non-zero temperature T and non-zero chemical potential μ.

3.1 Euclidean Space

Before we begin our discussion on lattice QCD it is worthwhile to consider how our field theory maps to Euclidean space, since the ability to do so is vital to lattice QCD. Recall the Minkowski metric:

$$\begin{aligned} x^\mu x_\mu &= x^\mu g^\nu_\mu x_\nu \\ &= \left(x^0\right)^2 - \left(x^1\right)^2 - \left(x^2\right)^2 - \left(x^3\right)^2, \end{aligned} \tag{10}$$

and the Euclidean metric:

$$\begin{aligned} x^\mu x_\mu &= x^\mu \delta^\nu_\mu x_\nu \\ &= \left(x^0\right)^2 + \left(x^1\right)^2 + \left(x^2\right)^2 + \left(x^3\right)^2. \end{aligned} \tag{11}$$

Consider the Wick rotation which maps $t \to -it = \tau$, i.e. $x^0 \to -ix^0$. Then the Minkowski metric transforms as:

$$\begin{aligned} x^\mu g^\nu_\mu x_\nu &= \left(x^0\right)^2 - \left(x^1\right)^2 - \left(x^2\right)^2 - \left(x^3\right)^2 \\ &\to -\left(x^0\right)^2 - \left(x^1\right)^2 - \left(x^2\right)^2 - \left(x^3\right)^2 \\ &= -x^\mu \delta^\nu_\mu x_\nu, \end{aligned} \tag{12}$$

which is the Euclidean metric up to a minus sign. So the Wick rotation maps Minkowski space to Euclidean space. We now consider how the path integral and the Dirac equation appears in Euclidean space.

For the path integral we need only consider the action $S = \int d^4x\, L$, where L is the Lagrangian density. Applying a Wick rotation we get:

$$dx^0 \to -idx^0, \tag{13}$$

$$\Rightarrow d^4x \to -id^4x, \tag{14}$$

$$\Rightarrow S \to -iS_E, \tag{15}$$

where the subscript E denotes a quantity in Euclidean space. Thus the path integral becomes

$$\begin{aligned} \langle O \rangle &= \frac{1}{Z} \int DA_\mu D\overline{\psi} D\psi \exp\left[-iS\right] O \\ &\to \frac{1}{Z} \int DA_\mu D\overline{\psi} D\psi \exp\left[-i\left(-iS_E\right)\right] O \\ &= \frac{1}{Z} \int DA_\mu D\overline{\psi} D\psi \exp\left[-S_E\right] O \\ &= \langle O \rangle_E. \end{aligned} \tag{16}$$

$$\text{where } Z = \int DA_\mu D\overline{\psi} D\psi \exp\left[-S_E\right]. \tag{17}$$

For the Dirac equation we have:

$$\begin{aligned} i\gamma^\mu D_\mu - m &= i\gamma^0 (\partial_0 + igA_0) + i\gamma^i (\partial_i + igA_i) - m \\ &\to i\gamma^0 (i\partial_0 + igA_0) + i\gamma^i (\partial_i + igA_i) - m \\ &= -\gamma^0 (\partial_0 + gA_0) + i\gamma^i (\partial_i + igA_i) - m \\ &= -\left(\gamma_E^0 (\partial_0 + igA_{E,0}) + \gamma_E^i (\partial_i + igA_{E,i}) + m\right) \quad (18) \\ &= -\left(\gamma_E^\mu D_\mu + m\right). \quad (19) \end{aligned}$$

where, in line (18) we made the substitutions:

$$\gamma^0 \to \gamma^0 = \gamma_E^0, \quad (20)$$
$$\gamma^i \to -i\gamma^i = \gamma_E^i, \quad (21)$$
$$A_0 \to iA_0 = A_{E,0}, \quad (22)$$
$$A_i \to A_i = A_{E,i}, \quad (23)$$

So

$$\begin{aligned} &-\left(\gamma_E^\mu D_\mu + m\right)\psi = 0 \\ &\Rightarrow \left(\gamma_E^\mu D_\mu + m\right)\psi = 0. \quad (24) \end{aligned}$$

The corresponding Lagrangian density is $L = \overline{\psi}\left(\gamma_E^\mu D_\mu + m\right)\psi$.
One can show (A.1) that the Euclidean gamma matrices satisfy the equations

$$\{\gamma_E^\mu, \gamma_E^\nu\} = 2\delta^{\mu\nu}, \quad (25)$$
$$(\gamma_E^\mu)^\dagger = \gamma^\mu. \quad (26)$$

Furthermore, for the matrix γ^5 defined as $\gamma^5 \coloneqq i\gamma^0\gamma^1\gamma^2\gamma^3$ we have:

$$\begin{aligned} \gamma^5 &= i\gamma^0\gamma^1\gamma^2\gamma^3 \\ &\to \gamma^0\gamma^1\gamma^2\gamma^3 \\ &= \gamma_E^5, \quad (27) \end{aligned}$$

which satisfies (see A.1):

$$\left\{\gamma^\mu, \gamma^5\right\} = 0, \quad (28)$$
$$\left(\gamma^5\right)^\dagger = \gamma^5, \quad (29)$$
$$\left(\gamma^5\right)^2 = 1. \quad (30)$$

3.2 Discretizing Spacetime

The lattice formulation is carried out by replacing the continuous set of points x^μ in Minkowski space by a discrete set of lattice points l^μ, where l^μ is a lattice vector.

Suppose the lattice is anisotropic, that is, the lattice spacing and number of lattice points varies in each of the $\left(x^0, x^1, x^2, x^3\right)$ directions. If we have N_μ lattice points with lattice spacing a_μ in the μ direction. Then we may write our points explicitly as:

$$\begin{aligned} x^\mu &\mapsto l^\mu, \\ l^\mu &= \left(a_0 n_0, a_1 n_1, a_2 n_2, a_3 n_3\right), \\ \text{where } 0 &\leq n_\mu \leq N_\mu - 1. \end{aligned} \tag{31}$$

In general, we choose the lattice spacing and number of lattice points along the spatial axes x^1, x^2, x^2 to be the same, which we will denote as a_s and N_s respectively. Furthermore we denote the spacing and number of lattice points along the temporal axis as a_t and N_t. With this notation it is convenient to define the anisotropy ξ, of the lattice as:

$$\xi \coloneqq \frac{a_s}{a_t}. \tag{32}$$

With this we may express our lattice vector l^μ as

$$\begin{aligned} l^\mu &= \left(a_t n_0, a_s n_1, a_s n_2, a_s n_3\right) \\ &= a_t \left(n_0, \xi \vec{n}\right). \\ \text{with } 0 &\leq n_0 \leq N_t - 1, \\ \text{and } 0 &\leq n_i \leq N_s - 1. \end{aligned} \tag{33}$$

It is more useful to write the lattice vector l^μ such that the temporal lattice spacing $a_t = a$ appears explicitly. To do this we write:

$$\begin{aligned} a n^\mu &= a_t \left(n_0, \xi \vec{n}\right) \\ &= l^\mu, \end{aligned} \tag{34}$$

with

$$a_s = a, \tag{35}$$

$$a_t = \frac{a}{\xi}. \tag{36}$$

3.3 Gauge Fields on the lattice

To determine how the gauge fields appear consider an operator of the form $\overline{\psi}(x)\psi(y)$. We wish to construct an operator of this type which is gauge invariant since it appears in the fermion action after discretization. To do this we first note how $\overline{\psi}(x)$ and $\psi(y)$ transform under a local gauge transformation. If $V(x)$ is an element of the gauge group $SU(N)$ assigned to the point x then:

$$\overline{\psi}(x) \mapsto \overline{\psi}(x) V^{-1}(x), \tag{37}$$

$$\psi(y) \mapsto V(y)\psi(y). \tag{38}$$

Now consider the operator $U(x,y) = \exp\left[igP\int_C dz^\mu A_\mu\right]$ where we are integrating over some open contour C with whose starting point is y and end point is x[1]. This transforms as (A.2):

$$U(x,y) \mapsto V(x) U(x,y) V^{-1}(y). \tag{39}$$

Thus the operator:

$$\overline{\psi}(x) U(x,y) \psi(y) \tag{40}$$

is gauge invariant. Formulating this on the lattice corresponds to the replacements $x^\mu \mapsto an^\mu$ and $y^\mu \mapsto am^\mu$. So on the lattice we have the gauge invariant term:

$$\overline{\psi}(an) U(an, am) \psi(am).$$

In particular, if an and am are adjacent lattice points, (i.e. $am = an + a\hat{\mu}$ where $\hat{\mu}$ is a unit lattice vector in the μ direction) then $U(an, an + a\hat{\mu})$ must be associated with the link moving from an to $an + a\hat{\mu}$ and is given by the equation:

$$U(an, an + a\hat{\mu}) = \exp\left[igP\int_C dz^\mu A_\mu\right]$$

where C is a contour from an to $an + a\hat{\mu}$. But due to lattice discretization the only contour between these two adjacent lattice points is a straight line, which we assign a constant gauge field A_μ to. Thus:

[1] The term P which appear in this expression denotes a path ordering, which is required since the gauge group is non-abelian

$$
\begin{aligned}
U\left(an, an + a\hat{\mu}\right) &= \exp\left[igP\int_{an}^{an+a\hat{\mu}} dz^{\mu} A_{\mu}\right] \\
&= \exp\left[iga_i A_{\mu}\right], \qquad (41) \\
\text{with } a_i &= \begin{cases} a_t \text{ if } \hat{\mu} \text{ points in the temporal direction.} \\ a_s \text{ if } \hat{\mu} \text{ points in a spatial direction,} \end{cases}
\end{aligned}
$$

From now on we denote $U_{nm} = \exp\left[iga_i A_{\mu}\right]$ to be the link variable associated with the link moving from lattice point an to the adjacent lattice point am. Furthermore, if U_{nm} is link from an to am, then its inverse must be the same link traversed in the opposite direction, i.e.:

$$
\begin{aligned}
U_{nm}^{-1} &= U_{nm}^{\dagger} \\
&= U_{mn}, \qquad (42)
\end{aligned}
$$

where $\dagger$ denotes the hermitian conjugate of an operator.

We are now left with determining which point we should assign the variable U_{nm}. Since the variables U_{nm} are assigned to the links between adjacent lattice points an and am, the point we choose should be in the vicinity of the link. The point chosen doesn't matter in the continuum limit, so we are free to choose any point we wish. For convenience we choose the midpoint between an and am.

Therefore, the gauge field A_{μ} appear on the lattice in the form of equation (41) as link variables between adjacent lattice points. The gauge measure becomes:

$$
DA_{\mu} \to \prod_{\{n,m\}} dU_{nm} = \left[dU\right], \qquad (43)
$$

where $\{n, m\}$ denotes a pair of adjacent lattice points an and am.

3.4 Fermions on the lattice

Before we discretize fermions on the lattice recall that fermionic fields anti-commute, i.e. they are Grassmann variables. Recall that a set G forms a Grassmann algebra if is satisfies the following conditions:

$$
\begin{aligned}
\theta_1\theta_2 &\in G \quad \forall\theta_1, \theta_2 \in G, \qquad (44) \\
\theta_1\theta_2 &= -\theta_2\theta_1 \quad \forall\theta_1, \theta_2 \in G, \qquad (45) \\
0 &\in G. \qquad (46)
\end{aligned}
$$

Some useful properties of Grassmann variables has been provided in the appendix (A.3).

With this in mind we now consider how fermions appear in the lattice formulation. This is done by virtue of the fact that the fermionic fields can be integrated out explicitly in Euclidean space. After mapping the fermionic integral to Euclidean space the solution reads (A.6):

$$\int D\overline{\psi}D\psi \exp\left[-iS_F\right] \rightarrow \int D\overline{\psi}D\psi \exp\left[-S_E\right]$$
$$= \det\left(M\right), \tag{47}$$
$$\text{where } M = \gamma_E^\mu D_\mu + m. \tag{48}$$

3.5 Lattice Actions

We now must choose an action to place on the lattice which determines the dynamics of the gauge and fermionic fields. From a theoretical standpoint, the lattice action chosen does not matter as long as its continuum limit converges to the QCD action. In the case of numerical simulations this is no longer true, since we cannot take a continuum limit when carrying out numerics. Thus there is a non-zero lattice spacing and a finite number of lattice points present in our simulation which introduces errors in the results, these errors are often referred to as lattice artifacts.[2]

Because of this, the lattice action chosen is non-trivial, as different actions will give rise to different lattice artifacts. Here we use two different sets of lattice actions, one for $SU\left(2\right)$ simulations and one for $SU\left(3\right)$ simulations.

- $SU\left(2\right)$: The Wilson gauge action and the Wilson fermion action
- $SU\left(3\right)$: The Symanzik improved Wilson gauge action and the Clover action

The continuum limit of the Wilson gauge and Wilson fermion actions have been presented in the appendix (A.4, A.5). Below we give explicit expressions for all the actions used, as well as the leading order corrections to these actions, which are proportional to the lattice spacing a.

The Wilson gauge action is given by:

[2] Lattice artifacts don't just refer to numerical uncertainties, but to more intrinsic problems associated with the lattice formulation e.g. fermion doubling, which won't be discussed here.

$$S_{\mathrm{WG}} = \sum_{\square} S_{\square} + \mathcal{O}(a) \text{ where } S_{\square} \text{ is the Plaquette action,} \tag{49}$$

$$S_{\square} = \frac{2N_c}{g^2}\left(1 - \frac{1}{N_c}\mathrm{tr}\left\{U_{n(n+a\hat{\mu})}U_{(n+a\hat{\mu})(n+a\hat{\mu}+a\hat{\nu})}U_{(n+a\hat{\mu}+a\hat{\nu})(n+a\hat{\nu})}U_{(n+a\hat{\nu})n}\right\}\right) \tag{50}$$

$$= S_{\mathrm{YM}} + \mathcal{O}\left(a^2\right), \tag{51}$$

where N_c is the number of colours present in the system and S_{YM} is the Yang-Mills action. The Wilson fermion action is:

$$S_{\mathrm{WF}} = \sum_n \sum_{\mu} \overline{\psi}_n \left(\psi_n + \kappa\left(1-\gamma_\mu\right)U_{n(n-a\hat{\mu})}\psi_{n-a\hat{\mu}} + \kappa\left(1+\gamma_\mu\right)U^{\dagger}_{n(n+a\hat{\mu})}\psi_{n+\hat{\mu}}\right) \tag{52}$$

$$= S_{\mathrm{F}}^{\mathrm{cont}} + \mathcal{O}(a). \tag{53}$$

Where κ is a parameter used to rescale the field ψ and $S_{\mathrm{F}}^{\mathrm{cont}}$ is the continuum fermion action. The Clover action is given by:

$$S_{\mathrm{c}} = S_{\mathrm{WF}} - \sum_n \sum_{\mu} \overline{\psi}_{n+a\hat{\mu}} \left(\frac{1}{2}c_{sw}\sum_{\nu<\mu}\left[\gamma_\mu,\gamma_\nu\right]F_{\mu\nu}\right)\psi_n \tag{54}$$

$$= S_{\mathrm{F}}^{\mathrm{cont}} + \mathcal{O}\left(a^2\right), \tag{55}$$

where c_{sw} is a coefficient chosen to maximize the $\mathcal{O}(a)$ correction to S_{WF} and:

$$F_{\mu\nu} = \frac{1}{8}\left(P_{\mu\nu} - P^{\dagger}_{\mu\nu}\right), \tag{56}$$

$$\begin{aligned} P_{\mu\nu} = {} & U_{n(n+a\hat{\mu})}U_{(n+a\hat{\mu})(n+a\hat{\mu}+a\hat{\nu})}U_{(n+a\hat{\mu}+a\hat{\nu})(n+a\hat{\nu})}U_{(n+a\hat{\nu})n} \\ & + U_{n(n+a\hat{\nu})}U_{(n+a\hat{\nu})(n-a\hat{\mu}+a\hat{\nu})}U_{(n-a\hat{\mu}+a\hat{\nu})(n-a\hat{\mu})}U_{(n-a\hat{\mu})n} \\ & + U_{n(n-a\hat{\mu})}U_{(n-a\hat{\mu})(n-a\hat{\mu}-a\hat{\nu})}U_{(n-a\hat{\mu}-a\hat{\nu})(n-a\hat{\nu})}U_{(n-a\hat{\nu})n} \\ & + U_{n(n-a\hat{\nu})}U_{(n-a\hat{\nu})(n+a\hat{\mu}-a\hat{\nu})}U_{(n+a\hat{\mu}-a\hat{\nu})(n+a\hat{\mu})}U_{(n+a\hat{\mu})n}. \end{aligned} \tag{57}$$

Finally the Symanzik improved Wilson gauge is:

$$
\begin{aligned}
S_{\mathrm{IWG}} &= S_{\mathrm{WG}} \\
&\quad - \alpha \sum_{n} \sum_{\mu,\nu<\mu} U_{n(n+a\hat{\mu})} U_{(n+a\hat{\mu})(n+2a\hat{\mu})} U_{(n+2a\hat{\mu})(n+2a\hat{\mu}+a\hat{\nu})} \times \\
&\quad U_{(n+2a\hat{\mu}+a\hat{\nu})(n+a\hat{\mu}+a\hat{\nu})} U_{(n+a\hat{\mu}+a\hat{\nu})(n+a\hat{\nu})} U_{(n+a\hat{\nu})n} \\
&\quad + c\alpha \sum_{n} \sum_{\mu,\nu<\mu,\rho<\nu} U_{n(n+a\hat{\mu})} U_{(n+a\hat{\mu})(n+a\hat{\mu}+a\hat{\nu})} \times \\
&\quad U_{(n+a\hat{\mu}+a\hat{\nu})(n+a\hat{\mu}+a\hat{\nu}+a\hat{\rho})} U_{(n+a\hat{\mu}+a\hat{\nu}+a\hat{\rho})(n+a\hat{\nu}+a\hat{\rho})} U_{(n+a\hat{\nu}+a\hat{\rho})(n+a\hat{\rho})} U_{(n+a\hat{\rho})n}, \\
&\quad = S_{\mathrm{YM}} + \mathcal{O}\left(a^6\right)
\end{aligned} \tag{58}
$$

where α and c are coefficients chosen to remove the $\mathcal{O}\left(a^2\right)$ errors in S_{WG}.

3.6 Monte Carlo Methods

Rewriting our Euclidean path integral on the lattice gives:

$$
\langle O \rangle_E = \frac{1}{Z} \int [dU] \exp\left[-S_E\right] \det\left(M\right) O, \tag{59}
$$

$$
\text{where } Z = \int [dU] \exp\left[-S_E\right] \det\left(M\right). \tag{60}
$$

We are now left with the task of calculating this integral numerically. Evaluating this integral using a mesh is impossible due to its massive dimension[3]. Instead we approximate this integral using Monte Carlo methods. To outline how this method works note that the $\det\left(M\right)$ is real and positive (A.7). Thus the quantity $\sigma\left(U\right) = \exp\left[-S_E\right] \det\left(M_E\right)$ is a positive function. So we have:

$$
\langle O \rangle_E = \frac{1}{Z} \int [dU] \, \sigma\left(U\right) O. \tag{61}
$$

The above expression may be thought of as an average over all field configurations of the operator O with a probability weight $\sigma\left(U\right)$. Such expressions are calculated via Monte Carlo methods by virtue of importance sampling, where only a small region of phase space contributes significantly to the integral, thus this integral may be well approximated by averaging over a relatively small collection of field configurations. This is done by starting with some initial

[3] For example, if we have an 8^4 lattice then there are $7,504$ links. If the gauge fields assigned to these links are elements of $SU\left(3\right)$ then the dimension of this integral is $8\left(7,504\right) = 60,032$ (since $SU\left(3\right)$ has 8 real parameters). Thus if we tried to evaluate this integral using a mesh with 10 points there would be $10^{60,032}$ terms to compute.

configuration C_1 and applying a random update to C_1 to generate a new configuration C_2. This process is repeated until we have a collection of configurations $\{C_1, ..., C_N\}$. The random update applied to our configurations is chosen such that the collection $\{C_1, ..., C_N\}$ converges to the ensemble $\sigma(U)$ as $N \to \infty$, where the uncertainty falls off as $\frac{1}{\sqrt{N}}$.

The more technical details of Monte Carlo methods relies on the notion of Markov Chains, which won't be discussed here (see [15]). The Monte Carlo algorithm used here will be the Hybrid Monte Carlo algorithm [14].

3.7 Lattice QCD at $T \neq 0$.

To introduce temperature consider a system in contact with a reservoir in thermal equilibrium at temperature T. The expectation value of an observable is then given by the partition function:

$$\langle O \rangle_T = \frac{\sum_n \exp\left[\frac{-E_n}{T}\right] O}{\sum_n \exp\left[\frac{-E_n}{T}\right]} \tag{62}$$

$$= \frac{1}{Z} \mathrm{tr}\left\{\exp\left[-\beta H\right] O\right\}, \tag{63}$$

with

$$\beta = \frac{1}{T}, \tag{64}$$

$$Z = \mathrm{tr}\left\{\exp\left[-\beta H\right]\right\}, \tag{65}$$

where we are summing over all states n with energy E_n and H is the Hamiltonian of the system. Using this one can show that (A.9):

$$\begin{aligned} \langle \psi(t,x)\, \psi(0,y) \rangle_T &= \langle \psi(-i\beta, y)\, \psi(t,x) \rangle_T \\ \Rightarrow \langle \psi(\tau,x)\, \psi(0,y) \rangle_T &= \langle \psi(\beta,y)\, \psi(\tau,x) \rangle_T, \end{aligned} \tag{66}$$

where we applied a Wick rotation $t \to -it = \tau$ in the second line. It follows that ψ must satisfy the boundary conditions:

$$\psi(0,x) = \pm \psi(\beta,x), \tag{67}$$

where the sign is determined by whether ψ is a bosonic$(+)$ or fermionic$(-)$ field.

To come to a field theory description of thermodynamics recall that the path integral formulation is given by:

$$\langle \psi(t_1)|e^{-iH(t_1-t_2)}|\psi(t_2)\rangle = \frac{1}{Z}\int D\psi \exp\left[i\int_{t_2}^{t_1} dt\, L\right] \tag{68}$$

$$\Rightarrow \langle \psi(t_1)|e^{-iH(-i\beta)}|\psi(t_2)\rangle = \frac{1}{Z}\int D\psi \exp\left[i\int_{0}^{-i\beta} dt\, L\right]. \tag{69}$$

In line (69) we made the substitution $t_1 - t_2 = -i\beta$. We again apply a Wick rotation to this expression and set $t_2 = 0$ to get:

$$\langle \psi(\beta)|e^{-iH\beta}|\psi(0)\rangle = \int D\psi \exp\left[-\int_0^{\beta} d\tau\, L_E\right], \tag{70}$$

but recall $\psi(0) = \pm\psi(\beta)$. Thus

$$\langle \psi(\beta)|e^{-iH\beta}|\psi(0)\rangle = \langle \psi(0)|e^{-iH\beta}|\psi(0)\rangle \tag{71}$$

$$= Z. \tag{72}$$

$$\Rightarrow Z = \int D\psi \exp\left[-\int_0^{\beta} d\tau\, L_E\right]. \tag{73}$$

Finally this gives us a field theory approach to thermodynamics:

$$\langle O\rangle_T = \frac{1}{Z}\int D\psi \exp\left[-\int_0^{\beta} d\tau\, L_E\right] O, \tag{74}$$

$$\beta = \frac{1}{T}. \tag{75}$$

So a system in thermal equilibrium at some finite temperature T may be formulated via a path integral carried out in Euclidean space on the interval $[0, \beta]$ where $\beta = \frac{1}{T}$. Furthermore the bosonic/fermionic fields are periodic/anti-periodic on this interval.

3.8 $\mu \neq 0$. The sign problem

We now introduce a non-zero chemical potential μ into our system. Recall that a system of N particles introduces a total energy of μN to the system, where $N = \int d^4x \psi^\dagger \psi$. Thus our action at finite chemical potential becomes:

$$S = \int d^4x \,\mathrm{tr}\left\{G^{\mu\nu}G_{\mu\nu}\right\} + \sum_f \overline{\psi}_f \left(i\gamma^\mu D_\mu - m_f\right)\psi_f \; + \mu N \tag{76}$$

$$= \int d^4x \,\mathrm{tr}\left\{G^{\mu\nu}G_{\mu\nu}\right\} + \sum_f \overline{\psi}_f \left(i\gamma^\mu D_\mu - m_f\right)\psi_f \; + \int d^4x \mu \psi^\dagger \psi \tag{77}$$

$$= \int d^4x \,\mathrm{tr}\left\{G^{\mu\nu}G_{\mu\nu}\right\} + \sum_f \overline{\psi}_f \left(i\gamma^\mu D_\mu - m_f + \gamma^0\mu\right)\psi_f. \tag{78}$$

With an analogous argument as the previous subsections, we have (in Euclidean space):

$$\langle O \rangle_E = \frac{1}{Z}\int [dU] \exp\left[-S_E\right] \det\left(M\left(\mu\right)\right) O. \tag{79}$$

$$M\left(\mu\right) = \gamma^\mu D_\mu + m_f + \gamma^0\mu. \tag{80}$$

To solve this expression using Monte Carlo methods we exploited the fact that $\det\left(M\right)$ was real. However, introducing a non-zero chemical potential now causes this quantity to become complex (A.7), rendering Monte Carlo methods useless.

To solve this we turn to 2 colour QCD, that is, a formulation of QCD whose gauge group is $SU\left(2\right)$ rather than $SU\left(3\right)$. In 2 colour QCD $\det\left(M\left(\mu\right)\right)$ is real for all values of chemical potential (A.8), leaving it amenable to Monte Carlo methods.

4 Definition of the static quark potential

4.1 The Thermal Wilsonloop

The definition of the static quark potential arises from the description of the late time dynamics of a heavy quark anti-quark pair. We do this via an Effective Field Theory (EFT) treatment of the $Q\overline{Q}$ system.

To begin we start with the full QCD Lagrangian density:

$$L_{QCD} = \mathrm{tr}\left\{G^{\mu\nu}G_{\mu\nu}\right\} + \sum_f \overline{\psi}_f \left(i\gamma^\mu D_\mu - m_f\right)\psi_f \tag{81}$$

$$= \mathrm{tr}\left\{G^{\mu\nu}G_{\mu\nu}\right\} + \sum_{lf} \overline{\psi}_{lf} \left(i\gamma^\mu D_\mu - m_{lf}\right)\psi_{lf} + \sum_{hf} \overline{\psi}_{hf} \left(i\gamma^\mu D_\mu - m_{hf}\right)\psi_{hf} \tag{82}$$

$$= L_G + L_{LQ} + L_{HQ}. \tag{83}$$

In line (83) we have split the QCD Lagrangian density in the gauge, light quark and heavy quark Lagrangian densities respectively.

We now neglect the light quark Lagrangian density and only consider the dynamics of the heavy quarks and gluons. Furthermore we suppress the sum over the heavy quark flavors and treat all heavy quark flavors as having the same mass m. This gives:

$$L_{QCD} = L_G + \overline{\psi}\left(i\gamma^\mu D_\mu - m\right)\psi. \tag{84}$$

To move to an EFT treatment, we apply a unitary transformation, known as the Foldy-Wuthuysen transformation, to our heavy quark Lagrangian density[4].Writing this up to leading order in $\frac{1}{m}$ gives [7]:

$$L_{NRQCD} = L_G + \chi^\dagger \left(iD_0 - m - \frac{\vec{D}^2}{2m} - \frac{g\vec{\sigma}.\vec{B}}{2m}\right)\chi + \phi^\dagger \left(iD_0 + m + \frac{\vec{D}^2}{2m} - \frac{g\vec{\sigma}.\vec{B}}{2m}\right)\phi \tag{85}$$

where σ^i are the Pauli matrices and $B^i = \epsilon^{ijk}F^{jk}$ is the colour magnetic field. The resulting EFT is known as non-relativistic QCD (NRQCD).

Note that we have written γ^μ in the Dirac representation so that we may identify $\psi = \begin{pmatrix}\chi\\ \phi\end{pmatrix}$, where $\chi^\dagger$ and $\phi^\dagger$ are Pauli spinor fields which create a quark and anti-quark respectively.

[4]To be more precise, we apply this transformation to the heavy quark Hamiltonian, then calculate the corresponding Lagrangian. Since we will be working entirely with the Lagrangian, we do not bother to include any Hamiltonian dynamics here.

In the infinite mass limit this yields:

$$L_{NRQCD} = L_G + \chi^\dagger \left(i\partial_0 + gA_0 - m \right) \chi + \phi^\dagger \left(i\partial_0 + gA_0 + m \right) \phi. \tag{86}$$

It has been shown (see [7]) that in this limit, the forward correlator for a $Q\overline{Q}$ pair, separated a spatial distance r , created at time $t = 0$ and annihilated at time t is given by the Wilsonloop formula:

$$\left\langle \phi\left(t,x\right) \chi\left(t,x+r\right) \chi^\dagger\left(0,x+r\right) \phi^\dagger\left(0,x\right) \right\rangle = \frac{1}{Z} \int DA_\mu e^{-iS_G} \mathrm{tr} \left\{ P \exp\left[\oint_C dx^\mu A_\mu \right] \right\} \tag{87}$$

$$= \frac{1}{Z} \int DA_\mu e^{-iS_G} W\left(r,t\right) \tag{88}$$

$$= \left\langle W\left(r,t\right) \right\rangle, \tag{89}$$

where $S_G = \int d^4x \, L_G$ is the gauge action and the Wilsonloop $W\left(r,t\right)$, is a rectangular loop in Minkowski space with temporal length t and spacial width r.

It is known that in thermal equilibrium, the Wilsonloop correlator obeys the equation[5][18]:

$$i\partial_t \left\langle W\left(r,t\right) \right\rangle = \Phi\left(r,t\right) \left\langle W\left(r,t\right) \right\rangle, \tag{90}$$

where $\Phi\left(r,t\right)$ is a complex function.

If the late time dynamics of the $Q\overline{Q}$ system may be described by some potential $V\left(r\right)$, then $\Phi\left(r,t\right)$ must converge to this potential as $t \to \infty$. This brings us to our definition of the static quark potential:

$$\begin{aligned} V\left(r\right) &:= \lim_{t\to\infty} \Phi\left(r,t\right) \\ &= \lim_{t\to\infty} \frac{i\partial_t \left\langle W\left(r,t\right) \right\rangle}{\left\langle W\left(r,t\right) \right\rangle}. \end{aligned} \tag{91}$$

Note that since $\Phi\left(r,t\right)$ is complex $V\left(r\right)$ is also complex.

[5]Note that we have dropped the subscript T for correlator in thermal equilibrium i.e. we wrote $\left\langle W\left(r,t\right) \right\rangle$ rather than $\left\langle W\left(r,t\right) \right\rangle_T$. From here on we will always neglect this subscript since all correlators are in thermal equilibrium for some $T \neq 0$.

4.2 Spectral Functions

To proceed with our calculation of the static quark potential we need to calculate the Wilsonloop correlator in Minkowski space. This poses a problem as the Monte Carlo methods used in lattice QCD are only applicable in Euclidean space. In other words, we cannot calculate $\langle W(r,t)\rangle$, but rather $\langle W(r,\tau)\rangle$ where $\tau = -it$.

To circumvent this we need to relate the Euclidean correlator to its Minkowski counterpart. We may do this by virtue of their spectral functions.

$$\langle W(r,t)\rangle = \int d\omega e^{-i\omega t}\rho(\omega,r)\,, \tag{92}$$

where $\rho(\omega,r)$ is the spectral function of $\langle W(r,t)\rangle$.

Recall that we can map Minkowski space to Euclidean space via a Wick rotation: $t \to -it$. Using this we have:

$$\langle W(r,t)\rangle \to \langle W(r,-it)\rangle = \langle W(r,\tau)\rangle\,. \tag{93}$$

Thus:

$$\begin{aligned}\langle W(r,t)\rangle &= \int d\omega e^{-i\omega t}\rho(\omega,r)\\ &\to \int d\omega e^{-\omega\tau}\rho(\omega,r)\\ &= \langle W(r,\tau)\rangle\,.\end{aligned} \tag{94}$$

Note from the above expression that $\langle W(r,t)\rangle$ and $\langle W(r,\tau)\rangle$ have the same spectral function $\rho(\omega,r)$. It is convenient to define $V(r)$ by virtue of the spectral function rather than the Wilsonloop. We can do this by combining equations (92) and (91):

$$\begin{aligned}V(r) &= \lim_{t\to\infty}\frac{i\partial_t\langle W(r,t)\rangle}{\langle W(r,t)\rangle}\\ &\lim_{t\to\infty}\frac{i\partial_t\int e^{-i\omega t}\rho(\omega,r)\,d\omega}{\int e^{-i\omega t}\rho(\omega,r)\,d\omega}\\ &= \lim_{t\to\infty}\frac{\int \omega e^{-i\omega t}\rho(\omega,r)\,d\omega}{\int e^{-i\omega t}\rho(\omega,r)\,d\omega}.\end{aligned} \tag{95}$$

With this definition it is now clear how we may calculate $V(r)$.

1. Calculate $\langle W(r,\tau)\rangle$ via lattice QCD
2. Use $\langle W(r,\tau)\rangle$ to infer $\rho(\omega,r)$
3. Calculate $V(r)$ by virtue of equation (95)

We finish with some remarks on how features of the spectral function $\rho(\omega,r)$ relate to $V(r)$.

From the functional form of equation (95) we can see that the lowest lying peak of the spectral function encodes information about the potential. In particular, it was thought that the peak position corresponded to the $\mathrm{Re}[V]$ while the peak width gave $\mathrm{Im}[V]$ [23].

It turns out this is not the case. Although $V(r)$ is defined in terms of the late time dynamics, the early time physics plays a role in how we can relate $V(r)$ to $\rho(\omega,r)$. To see this recall that $V(r) = \lim_{t\to\infty}\Phi(r,t)$. To study the effect of the early time scale we insert a complex function $\phi(r,t)$ such that $\phi(r,t)$ vanishes after some time t_0.

$$\Phi(r,t) = V(r) + \phi(r,t), \tag{96}$$
$$\phi(r,t) = 0 \,\mathrm{for}\, t > t_0. \tag{97}$$

Substituting this into equation (90) gives:

$$i\partial_t \langle W(r,t)\rangle = (V(r) + \phi(r,t))\langle W(r,t)\rangle. \tag{98}$$

We can solve this equation analytically, then invert equation (92) to obtain an expression for $\rho(\omega,r)$. Doing this yields[8]:

$$\rho(\omega,r) = \frac{1}{2\pi}\int_{-\infty}^{\infty} \exp\left[i\left(\omega - \mathrm{Re}[V(r)]\right)t - i\mathrm{Re}\left[\sigma(r,|t|)\right]\mathrm{sign}(t) - \left|\mathrm{Im}[V(r)]\,t\right| + \mathrm{Im}\left[\sigma(r,|t|)\right]\right]. \tag{99}$$

$$\sigma(r,|t|) = \int_0^t \phi(r,t')\,dt'. \tag{100}$$

The above expression may be rewritten in terms of a peak structure plus higher order corrections, expanded in terms of $(\omega - \mathrm{Re}[V(r)])\,t_0$:

$$\rho(\omega,r) = \frac{\exp[\mathrm{Im}[\Sigma(r)]]}{\pi}\left(\frac{|\mathrm{Im}[V(r)]|\cos(\mathrm{Re}[\Sigma(r)]) - (\mathrm{Re}[V(r)] - \omega)\sin(\mathrm{Re}[\Sigma(r)])}{\mathrm{Im}[V(r)]^2 + (\mathrm{Re}[V(r)] - \omega)^2}\right) \tag{101}$$
$$+ c_0(r) + c_1(r)\,t_0\,(\mathrm{Re}[V(r)] - \omega) + c_2(r)\,t_0^2\,(\mathrm{Re}[V(r)] - \omega)^2 + ..,$$

where $\Sigma(r) = \int_0^\infty \phi(r,t)\,dt$ and c_0, c_1, c_2 are expansion coefficients. So once we infer $\rho(\omega, r)$ form lattice simulations we can fit its lowest lying peak to equation (101) to extract $\mathrm{Re}[V(r)]$.

4.3 Bayesian Inference

We are now left with the task of inferring $\rho(\omega, r)$ from the Euclidean Wilsonloop $\langle W(r,\tau)\rangle$. If we knew the functional form of the Wilsonloop this could be done. However, since $\langle W(r,\tau)\rangle$ is calculated on the lattice rather than analytically, this is an ill-posed problem as we are trying to construct a smooth function from finite set of noisy data points.

To solve this we make use of Bayesian inference, which lets us reconstruct the most probable spectral function for a given data set. The basic principle underlying a method of Bayesian inference is that, given a data set D and a set of constraints I which the spectral function must satisfy, the probability of obtaining a spectral function ρ is given by $P[\rho|D,I]$. We wish to maximize this probability with respect to ρ. We can expand this expression by virtue of Bayes' Theorem:

$$P[\rho|D,I] = \frac{P[D|\rho,I]\,P[\rho|I]}{P[D|I]}, \tag{102}$$

$$\Rightarrow P[\rho|D,I] \propto P[D|\rho,I]\,P[\rho|I]\,. \tag{103}$$

Notice that $P[D|I]$ is a constant with respect to ρ, and thus, is irrelevant when maximizing $P[\rho|D,I]$. Hence we will focus our attention on the distributions $P[D|\rho,I]$ and $P[\rho|I]$.

First let us consider $P[D|\rho,I]$. Recall that our data set D contains noise, i.e. there is some inherent uncertainty in the data set from which we are trying in infer ρ. Because of this, it is more useful to consider D as an average over a distribution of possible data sets which could be obtained from ρ. Here we assume this distribution takes the form of a Gaussian distribution. Using this we can extract an expression for $P[D|\rho,I]$.

Suppose we select some spectral function ρ. From this we can calculate a corresponding data set D' by discretizing (92):

$$D'_j = \sum_i \Delta\omega_i \exp(-i\omega_i t_j)\,\rho(\omega_j)\,. \tag{104}$$

Since we assume our data sets are Gaussian distributed we can assign a probability to D' which reads:

$$\exp\left[-\frac{1}{2}\sum_{i,j}\left(D_i - D'_j\right)C^{-1}_{ij}\left(D_i - D'_j\right)\right], \tag{105}$$

where C_{ij} is the covariance matrix of D. This equation holds for any such data set D', in particular, it gives an explicit expression for the distribution of data sets about D. Thus:

$$P\left[D|\rho, I\right] = \exp\left[-\frac{1}{2}\sum_{i,j}\left(D_i - D'_j\right)C^{-1}_{ij}\left(D_i - D'_j\right)\right]. \tag{106}$$

We now move on to $P\left[\rho|I\right]$. This gives a distribution of all possible spectral functions which are characterized by the constraints I. The constraints placed on the spectral function can be determined from the underlying physics. In our case we know that the spectral function is smooth and positive. Using these it has been shown [9] that this distribution has the expression:

$$\begin{aligned} P\left[\rho \mid I\right] &= \int d\alpha P\left[\rho \mid \alpha, m\right] \\ &= \int d\alpha \frac{e^S}{\prod_{j=1}^{N} e^{\alpha\Delta\omega}\left(\alpha\Delta\omega_i\right)^{-\alpha\Delta\omega} m\left(\omega_i\right)\Gamma\left(\alpha\Delta\omega\right)}, \end{aligned} \tag{107}$$

with

$$S = \alpha\int d\omega\left(1 - \frac{\rho}{m} + \ln\left(\frac{\rho}{m}\right)\right), \tag{108}$$

where α is a parameter introduced to leave S dimensionless. The Bayesian inference method which uses this expression for $P\left[\rho|I\right]$ is known as the BR method.

5 Details of the Numerical Simulations and Results

Although the static quark potential is formulated in terms of the spectral function of Wilsonloop correlators, it has been found [10] that the spectral function of the Wilsonline correlator in the Coulomb gauge produces a lowest lying peak which is related to the static quark potential in precisely the same way the Wilsonloop is, that is, via equation (101). Due to the Wilsonline correlator offering a much better signal to noise ratio, we calculate the potential using this observable, rather than the Wilsonloop itself.

The Wilsonline correlators were measured from samples of lattice configurations generated at various values of temperature T and chemical potential μ. The correlators were also measured for a range of spatial separations $r \in \{a, 2a, .., 8a\}$ on the lattice between the quark anti-quark pair. Once this was done, the lowest lying peak of the correlators' spectral functions were inferred via the BR method outlined in (4.3). Finally, we fit the lowest lying peak of these spectral functions using the fit function (101) to extract a value for the $\mathrm{Re}\,(V)$.

Here the Wilsonline correlators were measured from two distinct samples of lattice configurations:

1. A set of high temperature lattice configurations generated in real QCD at $\mu = 0$ across a range of temperatures.
2. A set of 2 colour lattice configurations generated at a fixed temperature $T \neq 0$ across a range of chemical potentials.

5.1 High Temperature Analysis

5.1.1 Simulation parameters

The Wilsonline correlators were measured from lattice configurations each with $N_s = 24$ lattice points along the spatial axes and $N_\tau \in \{16, ..., 40\}$ lattice points on the temporal axis. Table 1 gives a summary of the lattice size, its temperature T in terms of the critical temperature $T_c = 185$MeV and the number of lattice configurations N_{conf}. We also display the lattice anisotropy $\xi = \frac{a_s}{a_\tau}$, the temporal and spatial lattice spacings a_τ and a_s, gauge coupling β and pion mass M_π. A more detailed outline of the lattice configurations can be found in [1].

Once the Wilsonline correlators were measured from each sample of lattice configurations, their spectral functions $\rho\,(\omega)$ were inferred via the BR method. A sample of these Wilsonline correlators is displayed in Figure 1 plotted on both linear and logarithmic scales with a relative uncertainty of $\frac{\Delta W}{W} \leq 10^{-3}$. From the logarithmic plots of the Wilsonline correlators, we can already see that an increase in temperature causes an increase in screening effects present in the

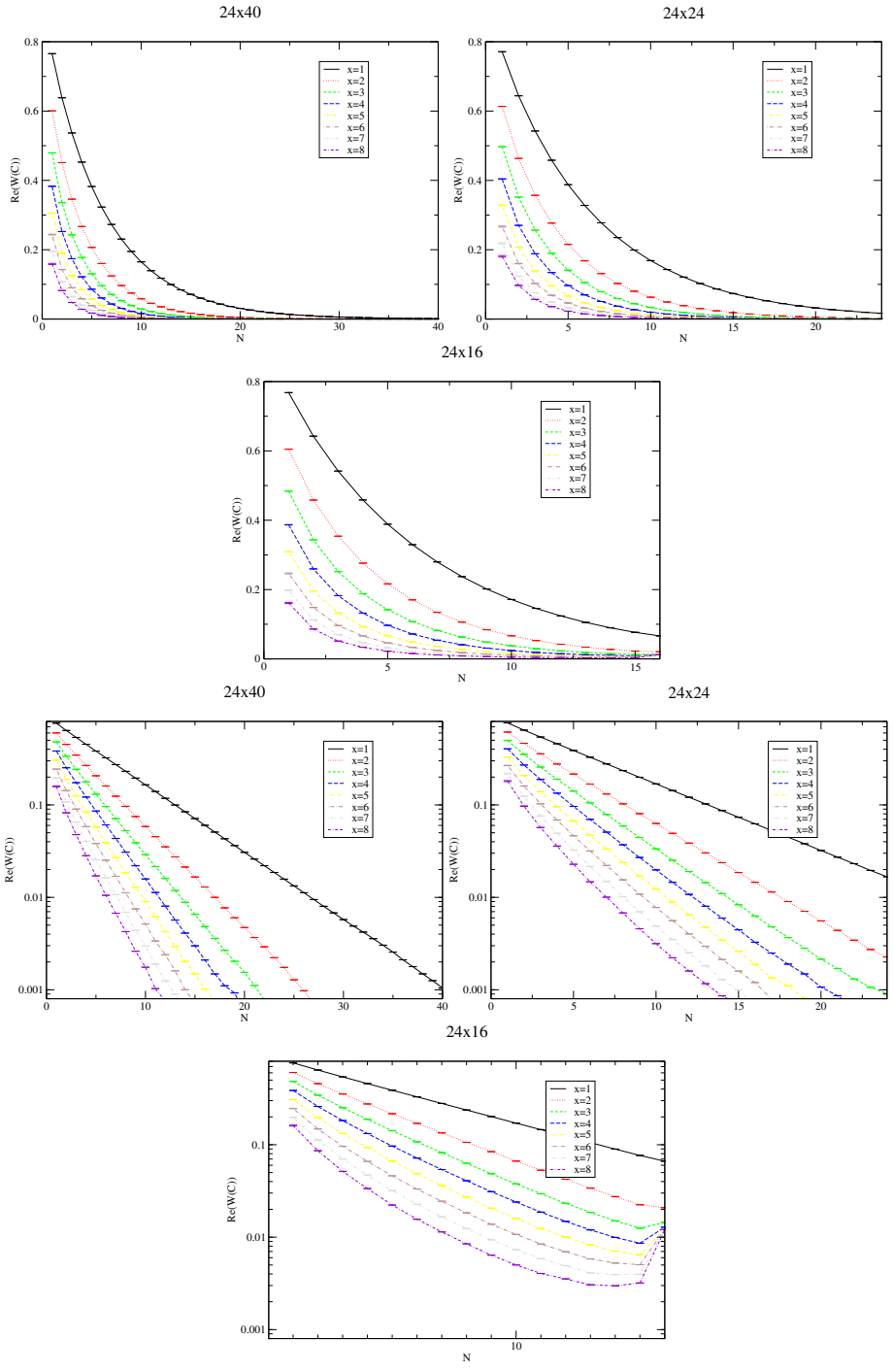

Figure 1: A sample of the Wilsonline correlators obtained from $N_\tau \in \{40, 24, 16\}$ data sets via lattice QCD. The top panel has been plotted on a linear scale, while the bottom panel as been plotted on a logarithmic scale.

Table 1: High temperature lattice configurations

$N_s^3 \times N_\tau$	$\frac{T}{T_C}$	N_{conf}	N_{jack}
$24^3 \times 40$	0.76	500	10
$24^3 \times 36$	0.84	496	16
$24^3 \times 32$	0.95	1000	10
$24^3 \times 28$	1.09	1000	10
$24^3 \times 24$	1.27	1000	10
$24^3 \times 20$	1.52	1000	10
$24^3 \times 16$	1.90	1000	10

ξ	a_τ	a_s	β	M_π
3.5	0.0351fm	0.123fm	1.5	384MeV

system by virtue of the decreasing slope of the correaltors with respect to temperature.

The spectral functions were reconstructed on the frequency range $\omega \in [-1, 5]$. The reconstruction was implemented three times for each spectral function, each time using a different model function $m(\omega)$. The model functions used were:

$$m_1(\omega) = \omega + 2, \tag{109}$$
$$m_2(\omega) = 1, \tag{110}$$
$$m_3(\omega) = \exp(1 - \omega). \tag{111}$$

Note that the ω is not the physical frequency but rather the frequency in lattice units, i.e. $\omega = \omega_{\text{phys}} a$. The uncertainty in the spectral functions was calculated using a Jackknife resampling. The number of Jackknife samples N_{jack} for each set of lattice configurations is also given in Table 1.

5.1.2 Results

Shown in Figure 2 are the reconstructed spectral functions from the Wilsonline correlators. The Wilsonlines were calculated for spatial distances $r \in \{a, 2a, .., 8a\}$. As such, each sample of lattice configurations yields 8 spectral functions, one for each value of spatial separation.The black, red and green graphs correspond to to the reconstructions using the model functions $m_1(\omega)$, $m_2(\omega)$ and $m_3(\omega)$ respectively.

From the results of the Bayesian inference we can see that as the temperature increases there is a flattening of the spectral function peaks. This peak flattening becomes more apparent as the spatial separation is increased. We can also see that the reconstruction appears quite stable with respect to the model function chosen, at least for low temperature reconstructions. In the high temperature

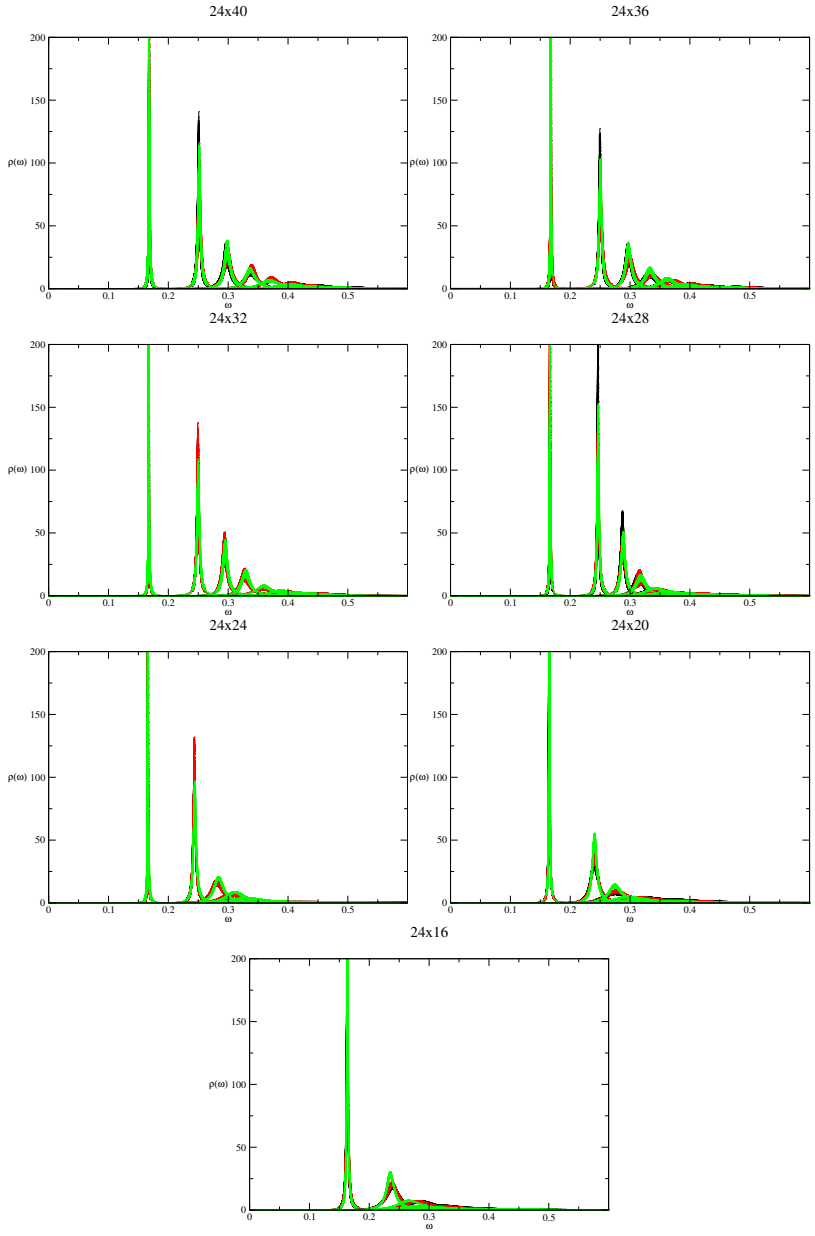

Figure 2: Spectral functions inferred from Wilsonline correlators via the BR method. Each figure contains spectral functions for each value of spatial separation $r \in \{a, .., 8a\}$, with the shortest separation yielding the lowest lying, narrow peak and the greatest separation yielding a wide peak positioned further along the ω axis.

results a discrepancy begins to appear, for example, in the $24^3 \times 16$ spectral functions, a distinction is already clear in the second spectral peak.

We now proceed to fit these peaks to extract a value for $\mathrm{Re}\,(V)$. The fit was carried out across the full width, half maximum of the spectral peak using the Levenberg-Marquardt fitting algorithm. Figures 3 and 4 display samples of the best fit graphs obtained by the fitting procedure from the $N_\tau = 36$ and $N_\tau = 16$ data sets respectively.

We determine the goodness of fit by virtue of the parameter $P\left(\chi^2\right)$ defined as:

$$P\left(\chi^2\right) \coloneqq \frac{\Gamma_{incomplete}\left(\frac{d}{2}, \frac{\chi^2}{2}\right)}{\Gamma\left(\frac{d}{2}\right)}, \tag{112}$$

where $\Gamma_{incomplete}$ is the incomplete gamma function, Γ is the gamma function, d is the number of degrees of freedom in the fit and χ^2 is usual chi squared parameter. The value of $P\left(\chi^2\right)$ lies between 0 and 1, with 1 corresponding to a perfect fit and 0 indicating a poor fit [22]. The $P\left(\chi^2\right)$ parameters are also displayed in Table 2.

$\frac{r}{a}$	1	2	3	4
$P\left(\chi^2\right)\left(24^3 \times 36\right)$	1	1	1	1
$P\left(\chi^2\right)\left(24^3 \times 16\right)$	1	1	1	1

Table 2: The $P\left(\chi^2\right)$ parameters for the $24^3 \times 36$ and $24^3 \times 16$ data sets for $r \in \{a, 2a, 3a, 4a\}$.

This fitting procedure was carried out on all spectral functions to extract a value for $\mathrm{Re}\,(aV)$ and $\mathrm{Im}(aV)$, where the potential has been measured in lattice units. Notice from Table 2 that we obtain a value of $P\left(\chi^2\right) = 1$ for all the fits displayed above, leading us to believe that we are over fitting the data. We attribute this over fitting to the large uncertainty present in the spectral reconstruction and the large number of fit parameters. Nevertheless, we proceed with the fit parameters obtained.

Figures 5 and 6 show the values of $\mathrm{Re}\,(aV)$ and $\mathrm{Im}\,(aV)$ respectively, plotted against $\frac{r}{a}$. Black, red and green indicates if the data point was extracted from a spectral peak reconstruction using the model function m_1, m_2 or m_3 respectively.

Before discussing the results for $\mathrm{Re}\,(aV)$ we will mention, in passing, $\mathrm{Im}(aV)$. From our understanding of the static quark potential we expect, up to leading order, a linear increase in $\mathrm{Im}\,(V)$ with respect to temperature [18]. We see from Figure 6 that there is an apparent increase in $\mathrm{Im}\,(aV)$ but this is difficult to to analyze quantitatively due to large uncertainty in $\mathrm{Im}\,(aV)$. Furthermore, Bayesian inference methods are known to be unreliable when inferring $\mathrm{Im}\,(aV)$. As such, we will not be discussing $\mathrm{Im}\,(aV)$ in this thesis, and only mention it here for the sake of completeness.

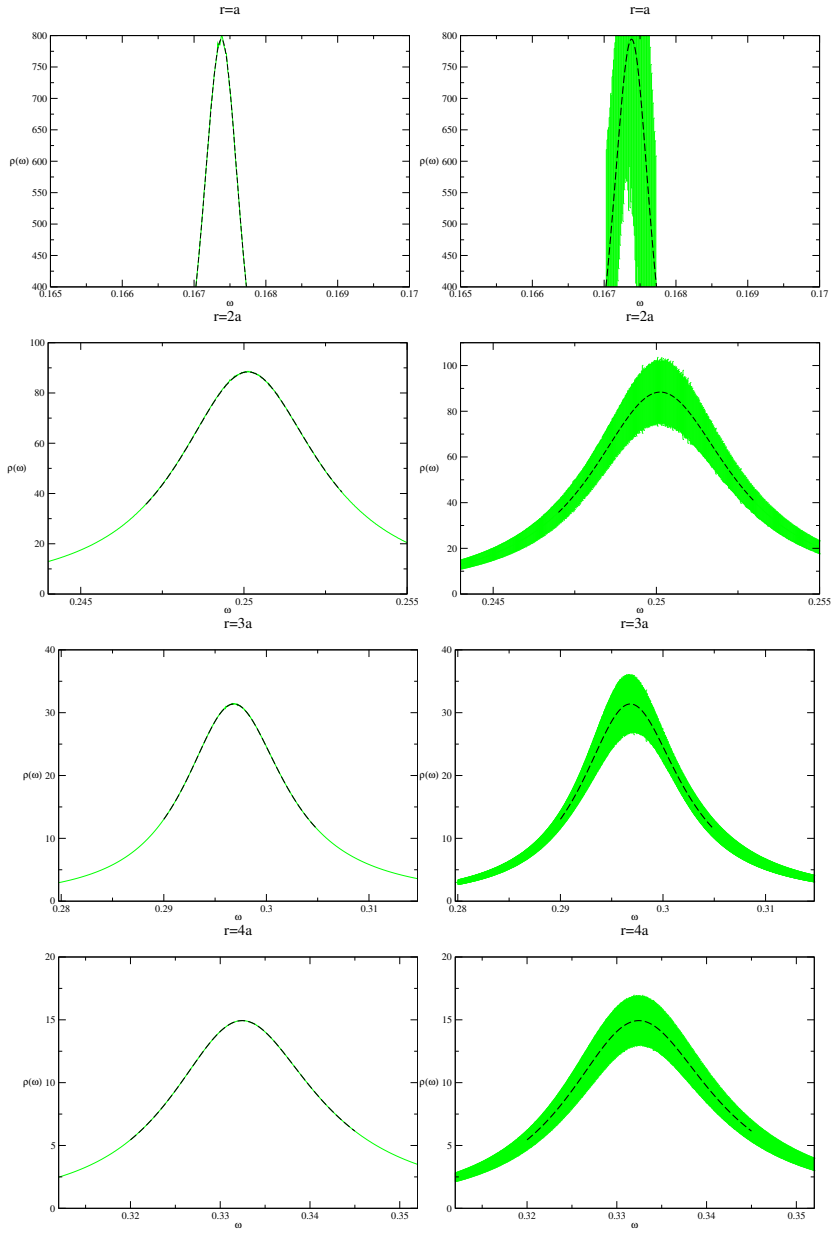

Figure 3: The best fit function of the lowest lying spectral peak for $r \in \{a, 2a, 3a, 4a\}$ reconstructed from the $24^3 \times 36$ configurations using the model function $m_3(\omega)$. The best fit function(black) is plotted on top of the original spectral peak(green). For the sake of clarity the functions are plotted twice, one plot displaying the uncertainty of the reconstructed spectral function.

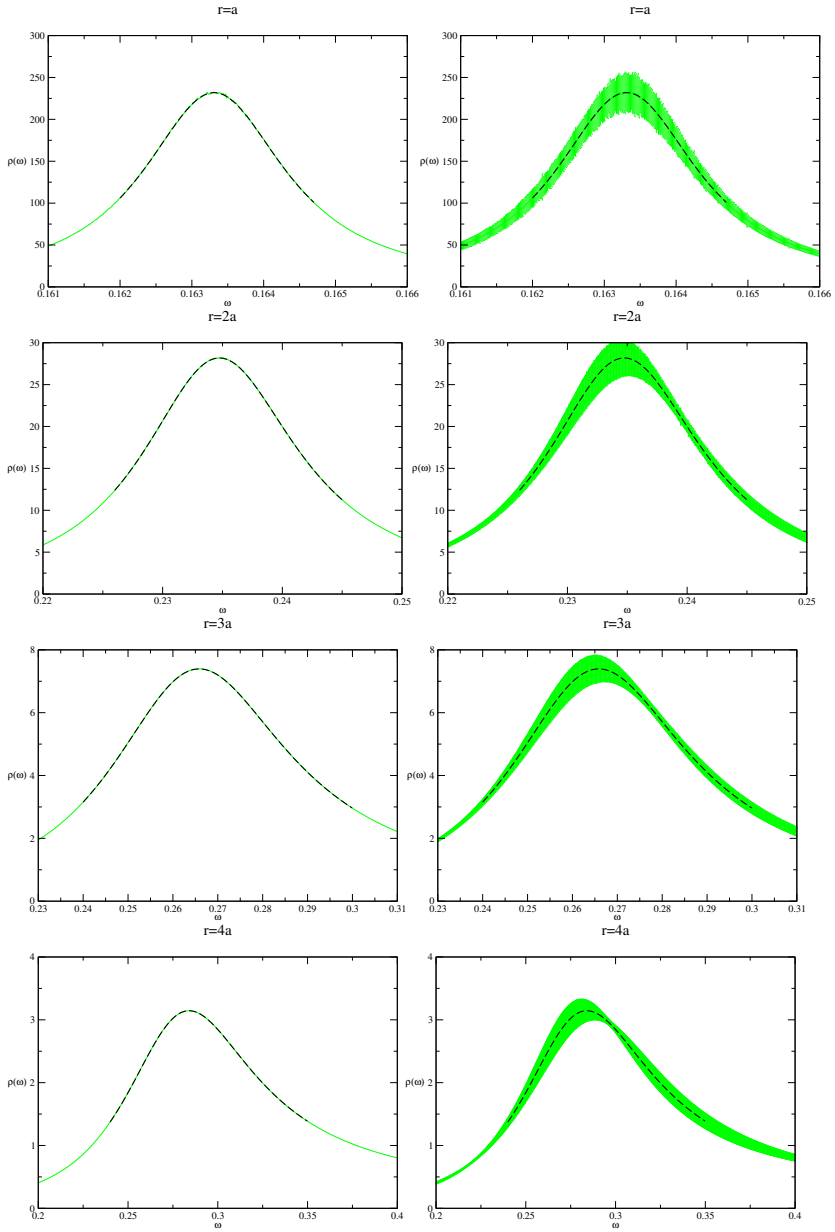

Figure 4: The best fit function of the lowest lying spectral peak for $r \in \{a, 2a, 3a, 4a\}$ reconstructed from the $24^3 \times 16$ configurations using the model function $m_3(\omega)$. The best fit function(black) is plotted on top of the original spectral peak(green). For the sake of clarity the functions are plotted twice, one plot displaying the uncertainty of the reconstructed spectral function.

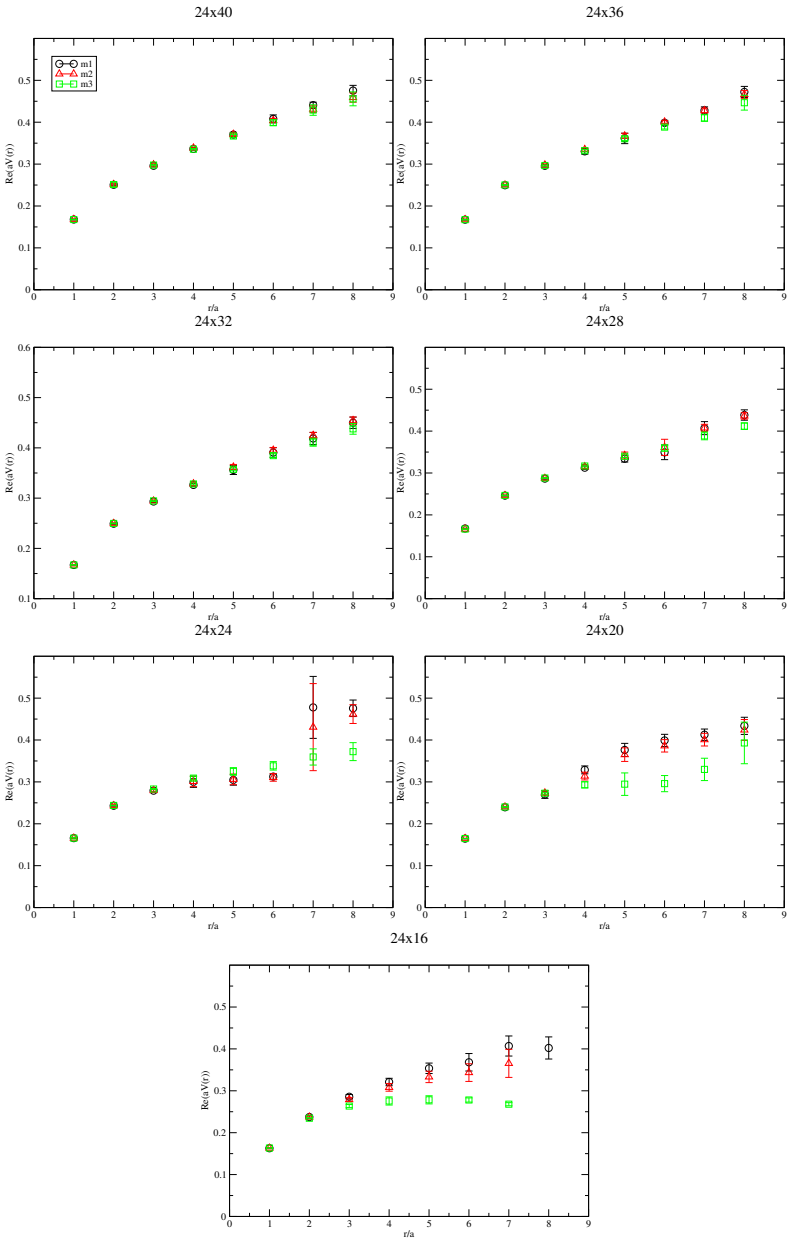

Figure 5: Values of $\mathrm{Re}\,(aV\,(r))$ extracted from the lowest lying peak of the spectral functions shown in Figure 2.

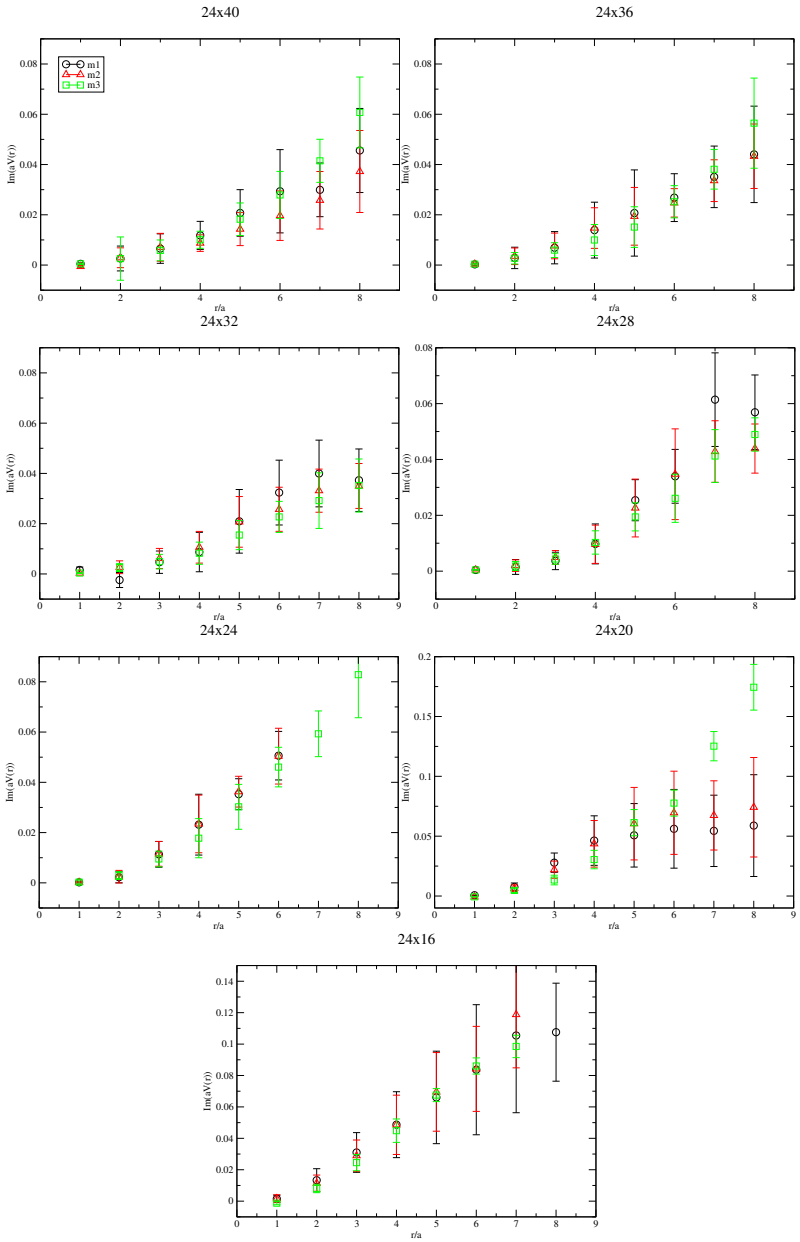

Figure 6: Values of$\mathrm{Im}\left(aV\left(r\right)\right)$ extracted from the lowest lying peak of the spectral function.

We now proceed to inspect the extracted values for $\mathrm{Re}\,(aV)$. We consider data points which are stable with respect to the model function, such as the ones seen in the $24^3 \times 40$ data set in Figure 5, to be reliable values for the $\mathrm{Re}\,(aV)$. On the other hand, unstable data points are seen as an indication that the lowest lying peak structure produced by the BR method is no longer trustworthy and these data points are neglected.

We can see this instability begin to take effect in the $24^3 \times 28$ sample in Figure 5, where a discrepancy begins to appear for $\frac{r}{a} = 6, 7, 8$. For $N_\tau = 20, 16$ we see that the values of $\mathrm{Re}\,(aV)$ are no longer reliable for distances larger than $\frac{r}{a} = 3$. We take this as a sign that for $\frac{r}{a} > 3$ the uncertainty in our data has become too large for the BR method to accurately reproduce the spectral peak. We refer the reader to [21], in which $\mathrm{Re}\,(aV)$ was successfully extracted via spectral function reconstruction at much larger temperatures. The simulation carried here uses much lower statistics than [21], which leads us to believe this is why the extraction breaks down for the highest temperature configurations.

Despite the numerical uncertainties there is still a clear flattening of the potential, which is particularly apparent at the $N_\tau = 28, 24$ data sets in Figure 5. Given that this flattening begins to occur at temperatures larger than T_c, we conclude that we are indeed observing the onset of deconfinement.

We finish our high temperature analysis by considering some potential models put forth in the literature. The first is the well known Cornell potential defined as:

$$\mathrm{Re}\,(V_{Cornell}(r)) \coloneqq \sigma r - \frac{\alpha}{r} + C. \tag{113}$$

The linear term in this potential model σr is associated with the confining nature of QCD. As such, the parameter σ is expected to decrease with both temperature and density, consistent with asymptotic freedom. The results of the fit are displayed in Figure 7. The fitted values for σa^2 and the $P\left(\chi^2\right)$ parameter are shown in Table 3. We do indeed observe a decrease in σ with the exception of the final two samples: $N_\tau = 20, 16$. The inconsistency in the final two samples is due to the data points in the $r \in \{3a, .., 8a\}$ range being unreliable and as a result, yielding a nonsensical fit.

N_τ	40	36	32	28	24	20
$\frac{T}{T_c}$	0.76	0.84	0.95	1.09	1.27	1.52
σa^2	0.0288(11)	0.0283(9)	0.0270(9)	0.0204(18)	0.0093(52)	0.0199(51)
$P\left(\chi^2\right)$	0.98448	0.9762	0.9759	0.8961	0.5711	0.2543

Table 3: The linear parameter σa^2 determined from fitting the Cornell potential

Secondly we consider the Karsch-Mehr-Satz model discussed in [17] given by:

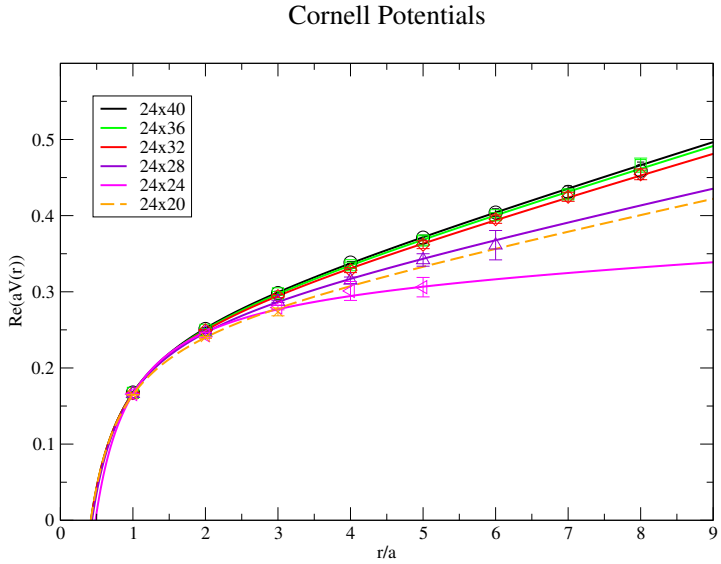

Figure 7: The graph produced by fitting the extracted values of $\mathrm{Re}\,(aV)$ to the Cornell potential model

$$\mathrm{Re}\,(V\,(r)):\;=\frac{\sigma}{m_{KMS}}\left(1-\exp\left(-m_{KMS}r\right)\right)+\left(-\frac{\alpha}{r}+C\right)\exp\left(-m_{KMS}r\right). \tag{114}$$

Note that we have modified the potential model found in [17] with the addition of the term $C\exp\left(-m_{KMS}r\right)$. This is due to the fact that the authors of [17] defined the Cornell potential such that the constant C does not appear. Since our definition of $V_{Cornell}$ differs slightly, we add this term to account for the discrepancy.

Furthermore, notice the introduction of the Debye mass, which we denote as m_{KMS} for this model, which is introduced to account for screening effects in the $Q\overline{Q}$ system caused by the surrounding thermal medium. Unlike the Cornell potential, the parameters σ, α and C determined at $T=0$ are considered constant with respect to temperature in this model, and any apparent change in the potential with respect to temperature is due to an increase in screening effects, i.e. an increase in m_{KMS}. Due to a lack of zero temperature Cornell parameters, we make do with treating the Cornell parameters of the lowest temperature i.e. the $24^3\times 40$ data set, as constant with respect to temperature. We then proceed to fit our extracted values for $\mathrm{Re}\,(aV\,(r))$ to this model in order to obtain a best fit value for am_{KMS}. The results are given in Figure 8 and Table 4.

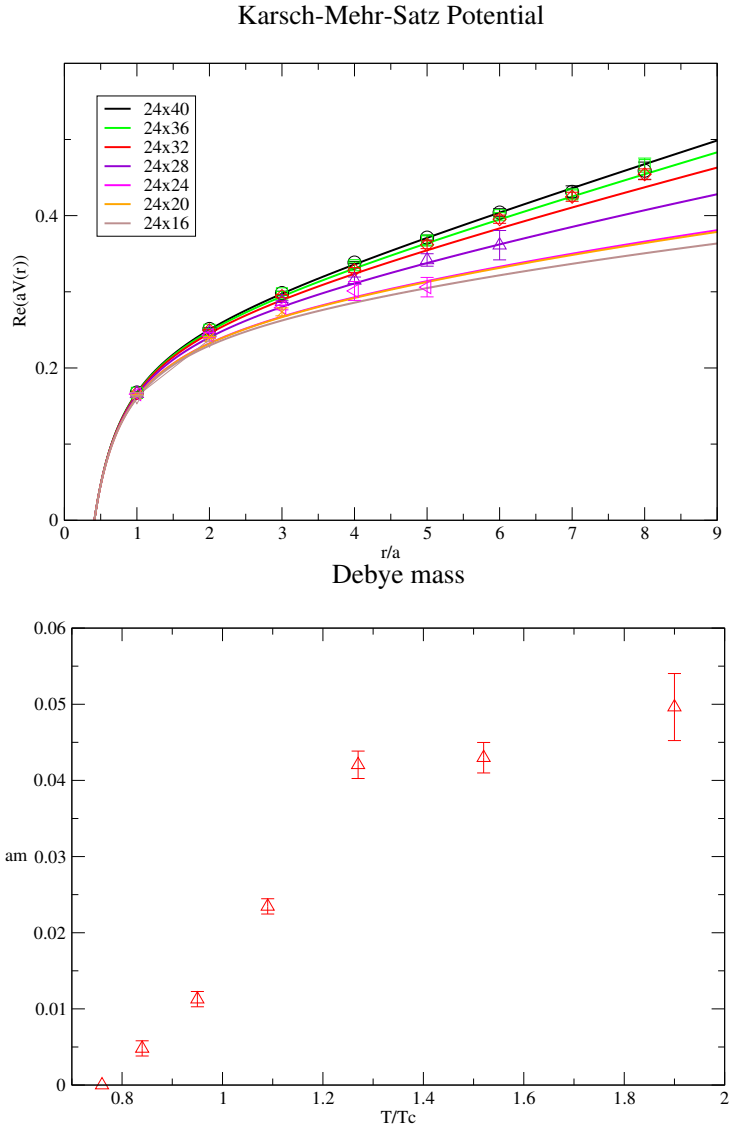

Figure 8: The screened potential as well as am_{KMS}, plotted as a function of $\frac{T}{T_C}$, determined from the Karsch-Mehr-Staz potential model

Table 4: Numerical values of $\frac{m_{KMS}}{T_c}$ determined from the Karsch-Mehr-Satz potential

N_τ	40	36	32	28	24	20	16
$\frac{T}{T_c}$	0.76	0.84	0.95	1.09	1.27	1.52	1.9
am_{KMS}	0	0.0048(1)	0.0113(1)	0.0235(1)	0.042(12)	0.043(2)	0.05(4)
$P\left(\chi^2\right)$	-	1.42×10^{-6}	8.0527×10^{-19}	2.617×10^{-15}	2.89×10^{-3}	4.8058×10^{-6}	6.66×10^{-3}

The values of $P\left(\chi^2\right)$ indicates quite a poor fit, so the fitted values of am_{KMS} need to be discussed cautiously. It is unclear if this poor fit is due to the short comings of the potential model or the fact that the Cornell parameters used were not the true zero temperature parameters. In any case there is an apparent increase in the Debye mass as a function of temperature. The increase is particularly large across the critical temperature T_c, consistent with deconfinement. There is an apparent plateau of the Debye mass for the higher temperature values. Given the lack of reliable data points for the high temperature data sets as well as the poor fit parameters, we dismiss this behavior as there is simply too much uncertainty to draw any meaningful conclusion for the highest temperature sets.

We finally finish with a more sophisticated potential model proposed in [11], which incorporates screening effects by treating the thermal medium surrounding the $Q\overline{Q}$ bound state as a weakly coupled gas. It reads:

$$\begin{aligned}\mathrm{Re}\left(V_{screened}\left(r\right)\right): \ =& -\alpha m_D - \alpha\frac{\exp\left(-m_D r\right)}{r} - \frac{\Gamma\left(\frac{1}{4}\right)\sigma^{\frac{3}{4}}\alpha^{\frac{1}{4}}}{2^{\frac{3}{4}}\sqrt{\pi m_D}} D_{-\frac{1}{2}}\left(\frac{\sqrt{2m_D}\sigma^{\frac{1}{4}}}{\alpha^{\frac{1}{4}}} r\right) \\ &+ \frac{\Gamma\left(\frac{1}{4}\right)\sigma^{\frac{3}{4}}\alpha^{\frac{1}{4}}}{2\Gamma\left(\frac{3}{4}\right)\sqrt{m_D}},\end{aligned} \tag{115}$$

where $\Gamma\left(z\right)$ is the usual gamma function, m_D denotes the Debye mass for this potential model and $D_v\left(z\right)$ is the parabolic cylinder function which, by definition, satisfies the differential equation

$$\frac{d^2}{dz^2} D_v\left(z\right) + \left(-\frac{1}{4}z^4 + \frac{1}{2} + v\right) D_v\left(z\right) = 0. \tag{116}$$

In a similar fashion to the fits above, we set $m_D = 0$ for the $24^3 \times 40$ sample to extract a best fit value for σ, α and C, then proceed to treat these as constant for all other data sets to deduce a value for m_D.

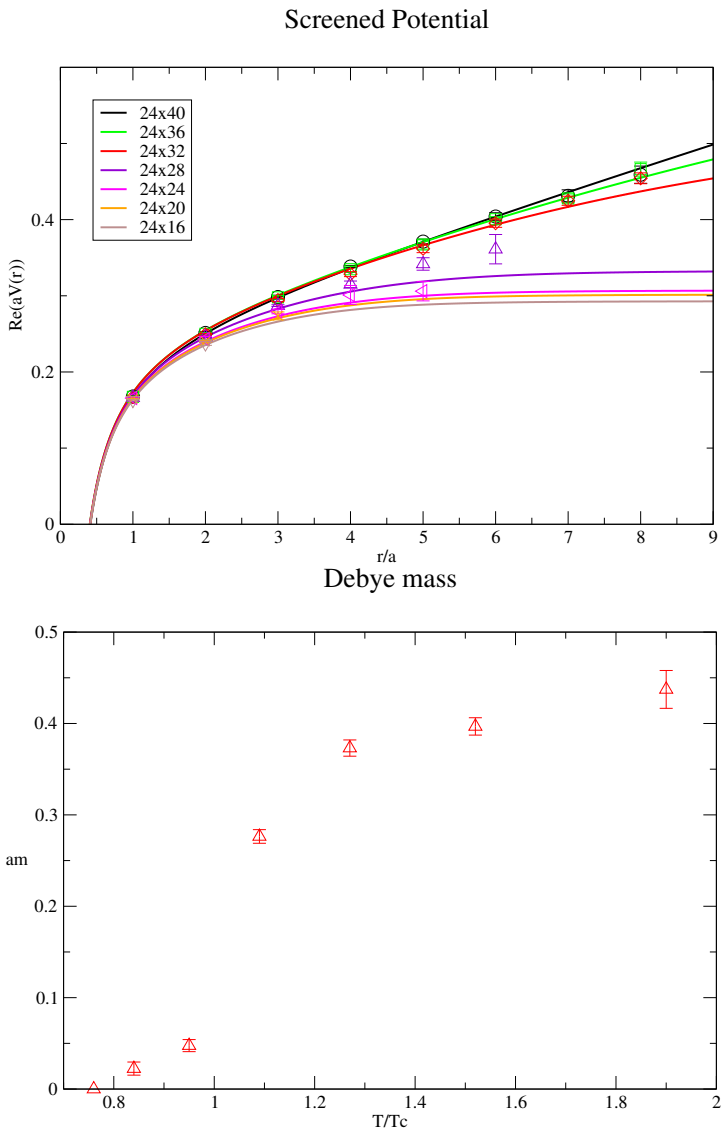

Figure 9: The screened potential and am_D plotted against $\frac{T}{T_C}$ obtained from potential model

Table 5: The numerical values of the Debye mass m_D

N_τ	40	36	32	28	24	20	16
$\frac{T}{T_c}$	0.76	0.84	0.95	1.09	1.27	1.52	1.9
am_D	0	0.0224(74)	0.0475(74)	0.2764(74)	0.3731(74)	0.3968(74)	0.4373(74)
$P(\chi^2)$	-	7.99×10^{-10}	3.435×10^{-41}	5.726×10^{-17}	0.1372	0.1104	0.2718

Once again we must take care with the goodness of fit. Similarly to the previous model we have extremely small values for the $P\left(\chi^2\right)$ parameter, at least for the low temperature data sets. Despite this we tentatively discuss the results of the fit.

Notice that the values of the Debye mass in this model behave in similar manner to the one obtained from the Karsch-Mehr-Satz model, that is, a noticeable increase in am_D across the transition temperature T_c. However, the values of am_D displayed in Table 5 are one order of magnitude larger compared to those displayed for am_{KMS} in Table 4. The Debye mass is associated with the screening effects present in a strongly interacting medium, and is thus considered to be a physically significant quantity. Because of this, one would expect $m_{KMS} \approx m_D$, however, we see that they appear to differ by one order of magnitude. This discrepancy may be accounted for in two ways.

Firstly, the Cornell parameters used were not true zero temperature parameters. It may be that the the Debye mass predicted by both models converge to similar values if lower temperature Cornell parameters are used. Secondly, there is ambiguity in the definition of the Debye mass.

In (114) the Debye mass is defined as the inverse length scale of the screening effects present in the system. The authors of [17] expect these screening effects to manifest themselves as an exponential decay in the potential and thus impose a prefactor of the form:

$$\exp\left(-\frac{r}{L}\right) = \exp\left(-m_{KMS}r\right). \tag{117}$$

Equation (115) on the other hand, tackles screening effects by virtue of Gauss's Law. In particular they relate the static quark potential to the colour electric field via the familiar equation:

$$\vec{E} = -\vec{\nabla}V, \tag{118}$$

they then impose screening effects on this colour electric field by introducing the permittivity of a weakly coupled gas to the colour charge distribution. In this case the permittivity is related to the Debye mass, up to leading order, by [24]:

$$\mathrm{Re}\left(\epsilon\right) = \left(1 - \frac{m_D^2}{p^2}\right), \tag{119}$$

$$\mathrm{Im}\left(\epsilon^{-1}\right) = \frac{-\pi T p m_D^2}{\left(p^2 + m_D^2\right)^2}. \tag{120}$$

Due to the more rigorous approach used to derive (115), we expect the values of m_D to be more physically relevant than m_{KMS}. However, due to a lack of data

points for large values of r in the high temperature data sets, we suspect that the fit functions obtained in Figure 8 are overestimating the screening effects present in the system. In particular, we don't expect such a drastic change in the potential energy between the $N_\tau = 32$ and $N_\tau = 28$ data sets. A similar analysis was carried out in [12] without such a drastic change being observed as well as obtaining similar values for the Debye mass. In [12], the authors made use of much finer lattices ($a_s = 0.097$fm) which allowed for the extraction of more long distance data points, which we believe, is why a more gradual change in the potential was observed across T_c.

5.2 Two Colour High Density Analysis

Here we present the results of a similar calculation carried out on dense two colour lattice configurations. Computations of the static quark potential in dense systems have been carried out previously by applying an exponential fit to the Wilsonloop correlator [16, 3]. A calculation of the static quark potential via the spectral function decomposition has (to the best of our knowledge) not been carried out. As such, it is interesting to compare our results to those found in [16, 3].

5.2.1 Simulation parameters

The 2 colour simulation was carried out in an analogous way to the high temperature analysis. The Wilsonline correlators were measured using lattice configurations generated on $16^3 \times 24$ lattices. The configurations were generated for chemical potentials $\mu\,(\text{MeV}) \in \{0, 333, 554, 776\}$. The Table 6 shows the chemical potential μ and the number of lattice configurations N_{conf} used in the Monte Carlo method as well as some of the lattice parameters used in the simulation. A more detailed outline of the lattice parameters can be found in [13]. We also display the number of Jackknife samples used in the BR method after the Wilsonline correlators were measured. Figure 10 displays the measured correlators plotted on both linear and logarithmic scales.

$N_s^3 \times N_\tau$	β	a	$\frac{m_\pi}{m_\rho}$	κ
$16^3 \times 24$	1.9	0.178fm	0.807	0.1680

μa	$\mu\,(\text{MeV})$	N_{conf}	N_{jack}
0	0	198	11
0.3	332	2000	10
0.5	554	2025	15
0.7	776	1530	16

Table 6: Details of the 2 colour lattice configurations as well as the chemical potential each sample was generated for

As we can see from Figure 10, there is much more noise present in the Wilsonline correlators than the high temperature simulation, particularly in the $\mu = 0$ data set. Furthermore there is no clear change in the correlators with increasing μ.

Once the Wilsonline correlators were measured we deployed the BR method with the model functions m_1, m_2 and m_3 used in the previous subsection given by equations (109),(110) and (111) respectively. The results of the Bayesian inference are displayed in Figure 11 with the black, red and green lines indicating reconstructions using m_1, m_2 and m_3 respectively.

The reconstructed spectral functions have similar characteristics to the ones seen previously, in particular, a lowest lying peak structure whose width and position increase with $\frac{r}{a}$. From the high temperature analyses presented in the previous subsection, one would expect spectral functions similar in shape to the ones seen for $\mu = 333$MeV and $\mu = 554$Mev. Because of this, the results of the $\mu = 0$ and $\mu = 776$MeV reconstructions are concerning. The $\mu = 0$ may be due to the low statistics available for the simulations (see Table 6). This clearly does not explain the $\mu = 776$MeV result since it was a relatively high statistics simulation.

The decrease in the magnitude of the first spectral peak for $\mu = 776$MeV as well as the almost flat peak structure for the $\frac{r}{a} = 2$ spectral function was not observed in the high temperature spectral peaks, even after the apparent onset of deconfinement was observed. As such, we suspect that this behavior is the result of lattice artifacts.

Nevertheless we proceed with fitting the peak structure of each spectral function to extract $\mathrm{Re}\,(V)$. These fits are displayed in Figures 12 and 13, while the extracted values for $\mathrm{Re}\,(V)$ are displayed in Figure 14.

$\frac{r}{a}$	1	2	3	4
$P\left(\chi^2\right)$ $(\mu = 333\text{MeV})$	1	1	1	1
$P\left(\chi^2\right)$ $(\mu = 776\text{MeV})$	1	1	1	1

Table 7: The $P\left(\chi^2\right)$ parameter for the $\mu a \in \{0.3, 0.7\}$ data sets for $r \in \{a, 2a, 3a, 4a\}$.

The results of the two colour analysis are not quite as satisfying as the high temperature results. First and foremost the numerical values for $\mathrm{Re}\,(aV)$ generally seem more unstable with respect to the model function. Furthermore, there is no obvious flattening of $\mathrm{Re}\,(aV)$ with increasing chemical potential. For completeness, we also fit these data points to the Cornell potential $V_{Cornell}\,(r)$. The best fit curves are presented in Figure 15. The numerical values of σ and the $P\left(\chi^2\right)$ parameters are shown in Table 8.

Due to asymptotic freedom, we might expect a decrease in σ with respect to μ but no such behavior is seen from our analysis. Indeed, the lowest value of μ has produced the lowest value of σ, while the largest value of μ has produced the largest value of σ, which almost perfectly contradicts what we expect to

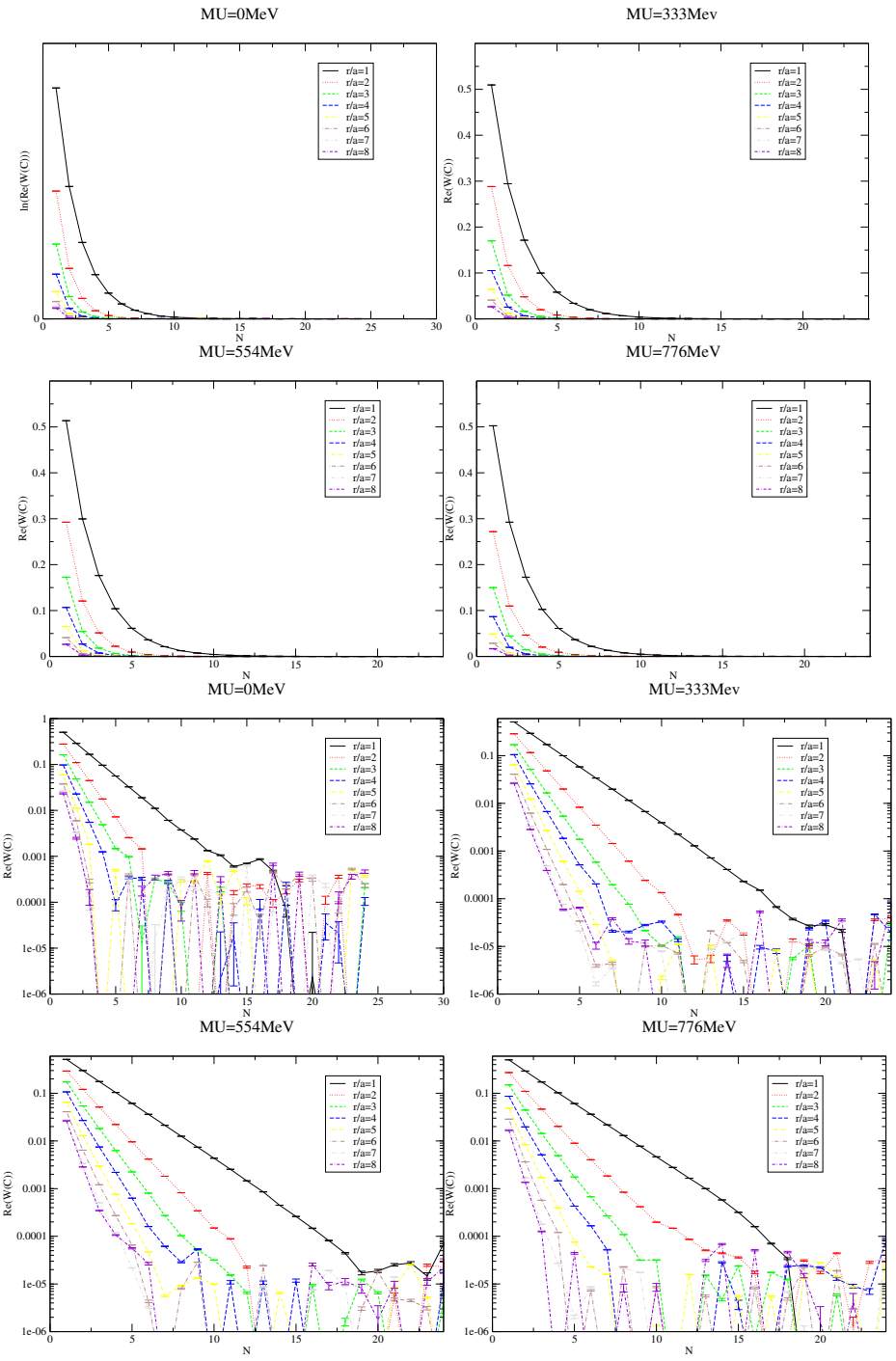

Figure 10: The Wilsonline correlators measured from the $\mu \in (0\text{MeV}, 333\text{MeV}, 554\text{MeV}, 776\text{MeV})$ 2 colour lattice configurations. The top panel has been plotted on a linear scale, while the bottom has been plotted on a logarithmic scale.

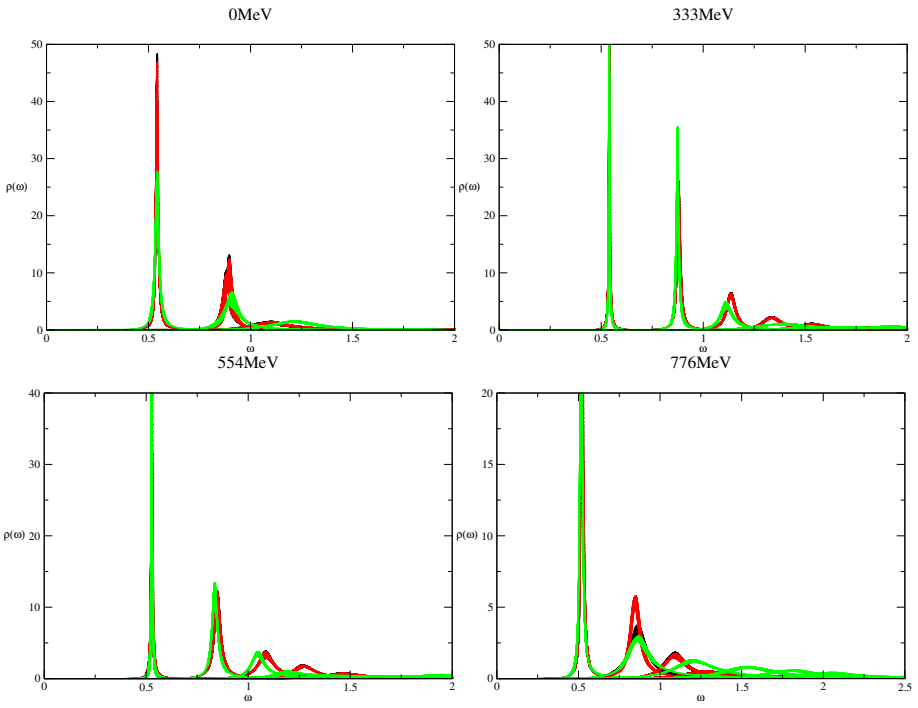

Figure 11: The spectral function reconstructions for $\mu a \in \{0, ..., 0.7\}$ at spatial separations $r \in \{a, ..., 8a\}$. The black, red and green graphs denote spectral functions reconstructed with m_1,m_2 and m_3 respectively.

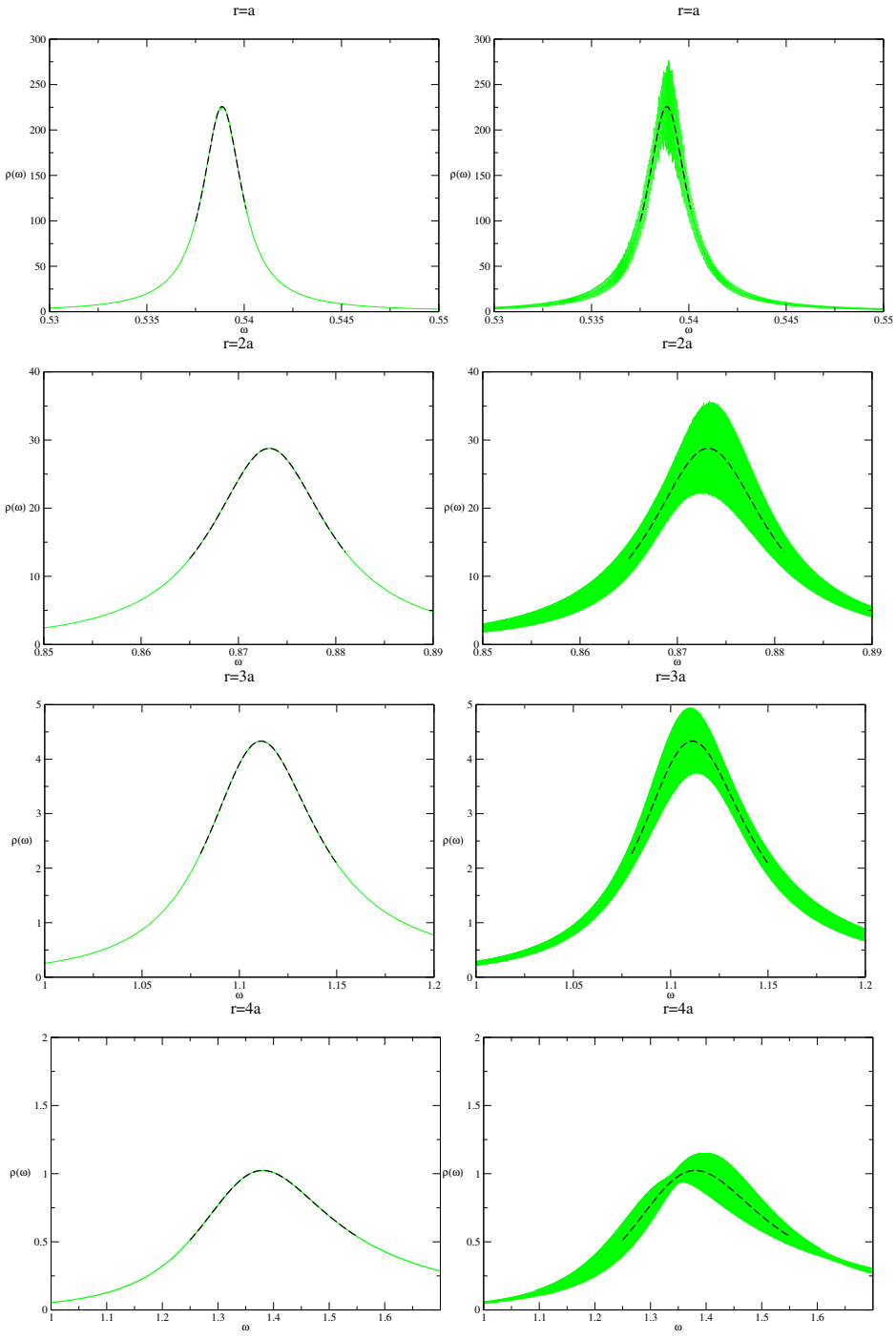

Figure 12: The fitted spectral peaks from the $\mu a = 0.3$ data set for spatial separations $r \in \{a, 2a, 3a, 4a\}$.

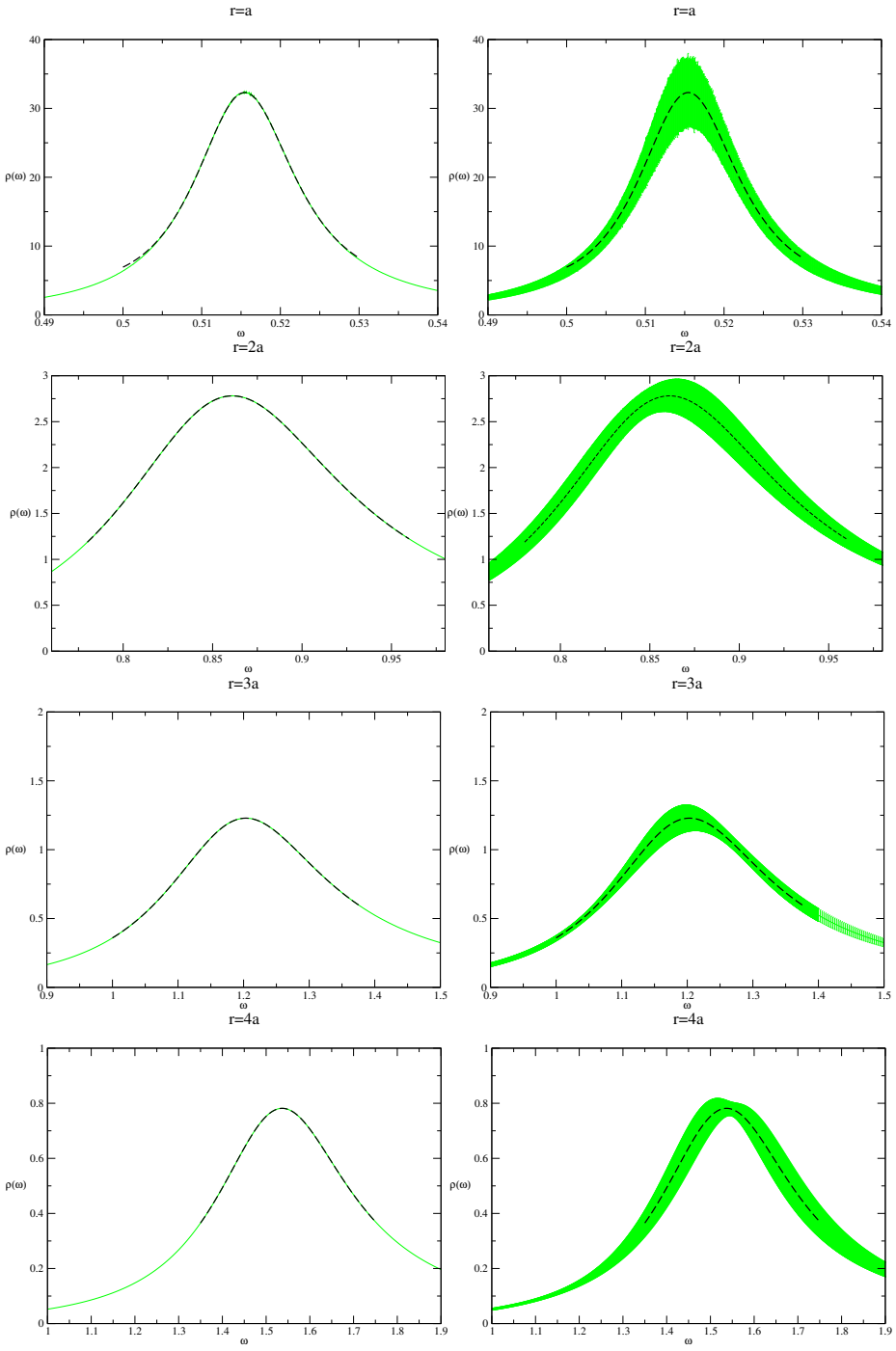

Figure 13: The fitted spectral peaks from the $\mu a = 0.7$ data set for spatial separations $r \in \{a, 2a, 3a, 4a\}$.

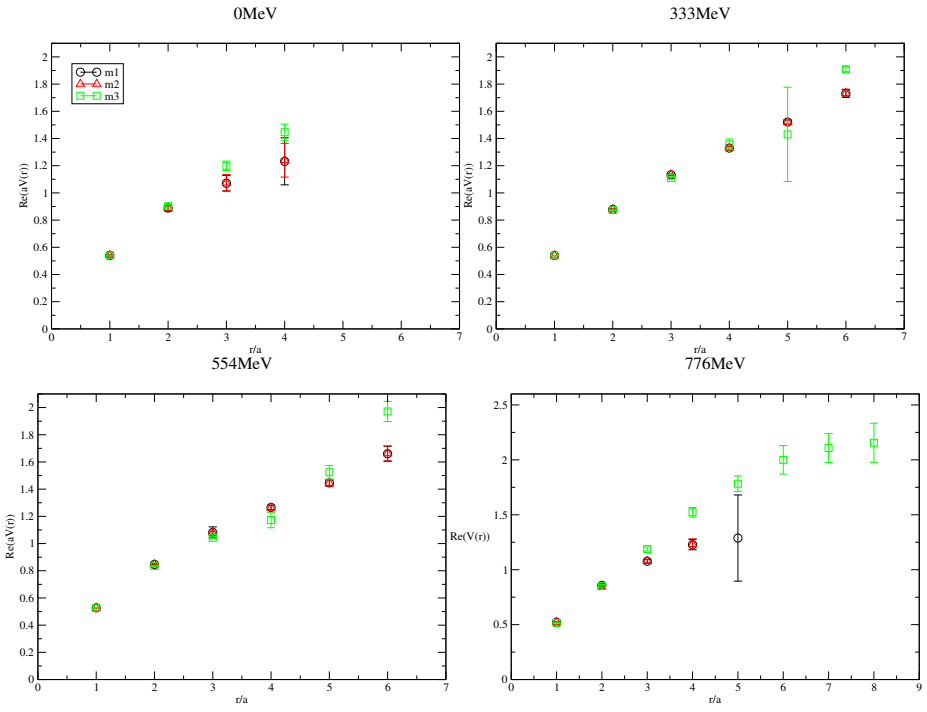

Figure 14: The values of $\mathrm{Re}\,(aV\,(r))$ extracted from the lowest lying spectral peaks shown in Figure 11.

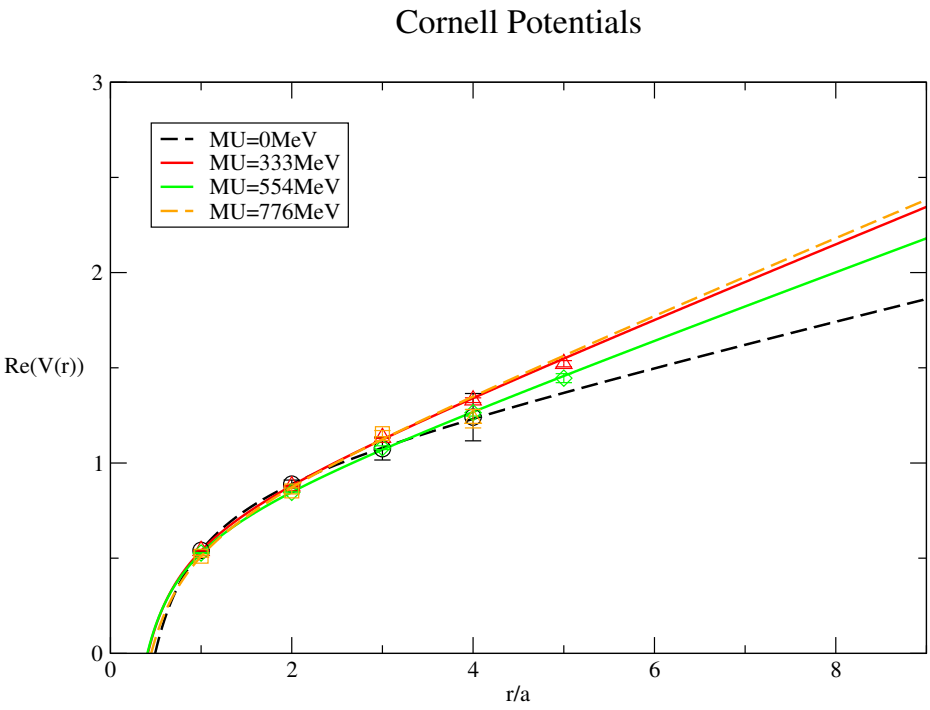

Figure 15: The graphs produced by fitting the extracted values of Re (V) to the Cornell potential model

μ(MeV)	0	333	554	776
$a^2\sigma$	0.1128(679)	0.1925(5)	0.1742(74)	0.197(17)
$P\left(\chi^2\right)$	0.914851	0.008988	0.456084	0.02245

Table 8: The values of the linear parameter σ determined from fitting the Cornell potential

observe. To determine the cause of this, we take a closer look at the lattice configurations used in the analysis.

Firstly, the $\mu = 0$MeV is a very low statistics simulation ($N_{\text{conf}} = 198$), which is reflected in the small number of data points extracted in Figure 14. Because of the large numerical uncertainty this produces in the extraction of Re (V), we suspect that the results for $\mu = 0$ are not physically relevant. It is worth noting, however, that the large uncertainty in σa^2 for $\mu = 0$ is consistent with the value of σa^2 obtained for $\mu = 332$MeV, so there appears to be no statistically significant change in σ in this range of density.

As for the $\mu = 776$MeV data set, we suspect that lattice artifacts are corrupting the results. This is reflected in the spectral reconstruction for $\mu = 776$MeV in Figure 11, where the BR method produced far more peak structures for the model function m_3 than m_1 and m_2. The results from the $\mu a \in \{0.3, 0.5\}$

appear reliable and indicate a flattening of the potential with increasing chemical potential. From the values of σ extracted from these results, it appears that deconfinement does not occur across this range of densities.

The numerical values of $\mathrm{Re}\,(V)$ for $\mu a \in \{0.3, 0.5\}$ displayed in Figure 11 agree reasonably well with those found in [3]. The numerical methods and lattice sizes used in [3] differ from ours, but all other lattice parameters (ξ, a_s, a_τ, etc.) are the same, which demonstrates that the numerical methods used here are indeed reliable. An analysis of the free energy between a quark anti-quark pair was carried out in [2] on much finer lattices ($a = 0.044$fm) with an improved Symanzik gauge action and a staggered fermion action. In [2] deconfinement was observed via the free energy at higher densities ($\mu \approx 1$GeV) than the ones available here. Hence our results are consistent with what has been found in previous analyses.

For the sake of completeness we will also fit these data points to the Karsch-Mehr-Satz model defined in (114). The fitting procedure we carry out here is slightly different to the one used in the high temperature analysis. When carrying out the potential fits in the previous subsection we treated the zero temperature Cornell parameters as constants with respect to temperature and proceeded to fit only the Debye mass parameter m_{KMS}. Ideally, we would treat the zero density Cornell parameters as constants here too, however, due to the large uncertainty in the $\mu = 0$Mev results, this is not feasible, so we make do with fitting to all four parameters, σ, α, C and m_{KMS}. The best fit functions are given in Figure 16, with σ, m_{KMS} and $P\left(\chi^2\right)$ parameters shown in Table 9.

μa	0	0.3	0.5	0.7
am_{KMS}	-0.2188	0.1534	0.1139	0.4503
σa^2	-0.1848	0.3911	0.3174	0.6803
$P\left(\chi^2\right)$	-	0.349851	0.554802	-

Table 9: The numerical values of m_{KMS} and σ obtained from the Karsch-Mehr-Satz model

We cannot determine a $P\left(\chi^2\right)$ parameter for $\mu a \in \{0, 0.7\}$ since there are no degrees of freedom when fitting these data sets. As expected these data sets produce nonsensical fits, such as a negative Debye mass seen in the $\mu a = 0$ fit or a large increase in σ for $\mu a = 0.7$. The fits $\mu a \in \{0.3, 0.5\}$ produce an apparent decrease in the Debye mass parameter. We attribute this to the fact that we are using non-constant Cornell parameters for this fit. For these reasons we cannot draw any meaningful conclusion from this potential model fit.

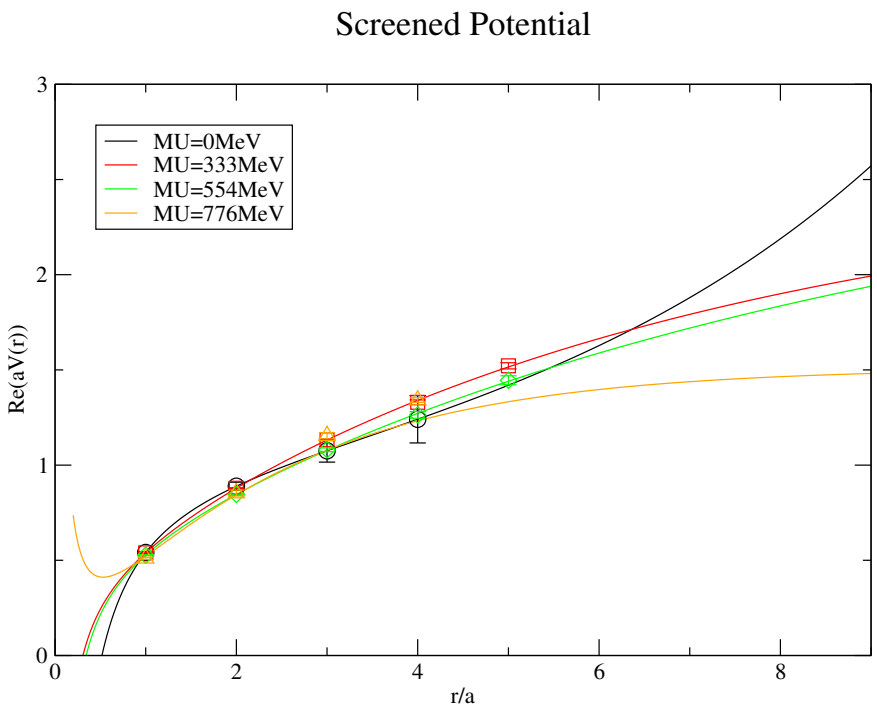

Figure 16: The Karsch-Mehr-Satz potential model fitted to the 2 colour potential for $\mu a \in \{0.3, 0.5, 0.7\}$

6 Conclusions

The static quark potential has a long history in heavy quark physics. Despite this the real time potential is still in relative infancy, particularly in dense systems and to a lesser extent, high temperature systems. Originally the problem has been approached using suitable ansatz for the potential energy and in more recent years, an EFT approach. With the formulation of this new Bayesian inference method we are finally able to infer numerical values of $V(r)$ from the underlying theory.

At high temperature we have observed the onset of deconfinement by virtue of the flattening of the static quark potential. The Bayesian inference method used produced fewer reliable data points for the $\mathrm{Re}(V)$ from the highest temperature lattice configurations. This was due to fewer lattice points N_τ being available along the temporal axis. As such we expect that a finer lattice spacing is required to numerically infer $\mathrm{Re}(V)$ at higher temperatures.

From the two colour analysis, no deconfinement was observed across the range of densities available to us. This is consistent with a previous investigation on dense quark matter where deconfinement was observed at higher densities [2]. Due to the corruption of the results by lattice artifacts, it is crucial that improved lattice actions are implemented moving forward. Despite this, we obtained values for $\mathrm{Re}(V)$ similar to the ones found in [3], which serves as an ideal cross examination of the numerical methods used in both calculations.

Acknowledgments We thank J.I. Skullerud for supervising this research project as well as investing a substantial amount of time into making this thesis a reality. We also thank A.Rothkopf for providing the Wilsonline and Bayesian inference software, as well as helpful insights into the underlying theory. The high temperature lattice configurations were provided by the FASTUM collaboration and the two colour lattice data was provided by the Maynooth-Swansea two colour project.

Appendix

A Lattice QCD

A.1 γ_E^μ algebra

We derive the anti-commutation relations of the Euclidean gamma matrices γ_E^μ, γ_E^5 and their Hermitian conjugates where:

$$
\begin{aligned}
\gamma_E^0 &= \gamma^0, \\
\gamma_E^i &= -i\gamma^i, \\
\gamma_E^5 &= \gamma^0\gamma^1\gamma^2\gamma^3.
\end{aligned}
$$

We determine the anti-commutator of the Euclidean gamma matrices via the anti-commutation relations of their Minkowski counterparts. Recall that the gamma matrices in Minkowski space satisfy the relations:

$$
\begin{aligned}
\{\gamma^\mu, \gamma^\nu\} &= 2g^{\mu\nu}, \\
\left\{\gamma^5, \gamma^\mu\right\} &= 0, \\
(\gamma^\mu)^\dagger &= \gamma^0\gamma^\mu\gamma^0, \\
\left(\gamma^5\right)^\dagger &= \gamma^5.
\end{aligned}
$$

Using these we have:

$$
\begin{aligned}
\left\{\gamma_E^0, \gamma_E^i\right\} &= \left\{\gamma^0, -i\gamma^i\right\} \\
&= 2g^{0i} \\
&= 2\delta^{0i}. && (121) \\
\left\{\gamma_E^j, \gamma_E^i\right\} &= \left\{-i\gamma^j, -i\gamma^i\right\} \\
&= -\left\{\gamma^j, \gamma^i\right\} \\
&= -2g^{ji} \\
&= 2\delta^{ji}. && (122) \\
\left\{\gamma_E^0, \gamma_E^0\right\} &= \left\{\gamma^0, \gamma^0\right\} \\
&= 2g^{00} \\
&= 2\delta^{00}. && (123)
\end{aligned}
$$

These can be written more compactly as

$$
\{\gamma_E^\mu, \gamma_E^\nu\} = 2\delta^{\mu\nu}. \tag{124}
$$

Furthermore

$$
\begin{aligned}
\left(\gamma_E^i\right)^\dagger &= \left(-i\gamma^i\right)^\dagger \\
&= -i\gamma^i \\
&= \gamma_E^i, && (125) \\
\Rightarrow (\gamma_E^\mu)^\dagger &= \gamma_E^\mu. && (126)
\end{aligned}
$$

Now for $\gamma_E^5 = \gamma^0\gamma^1\gamma^2\gamma^3$:

$$\left\{\gamma_E^5, \gamma_E^i\right\} = \left\{\gamma^5, -i\gamma^i\right\} = 0, \tag{127}$$
$$\left\{\gamma_E^5, \gamma_E^0\right\} = \left\{\gamma^5, \gamma^0\right\} = 0, \tag{128}$$
$$\left\{\gamma_E^5, \gamma_E^\mu\right\} = 0. \tag{129}$$

And:

$$\left(\gamma_E^5\right)^\dagger = \left(\gamma^5\right)^\dagger = \gamma^5 = \gamma_E^5. \tag{130}$$

A.2 Gauge transformation of $U(x,y)$

We wish to show that $U(x,y)$ transforms as $U(x,y) \to V(x)\,U(x,y)\,V^{-1}(y)$ under local gauge transformations.

By definition, we have $U(x,y) = \exp\left[igP\int_C A_\mu dz^\mu\right]$, where C is some open contour with parametrization $z^\mu(s)$ such that $z^\mu(1) = x$ and $z^\mu(0) = y$ for $s \in [0,1]$. To determine the transformation law of U we consider the case when the end point x is no longer fixed, i.e. we have $x(\alpha) = z^\mu(\alpha)$ for some $\alpha \in [0,1]$. Then:

$$U(x(\alpha), y) = \exp\left[igP\int_0^\alpha A_\mu \frac{dz^\mu}{ds} ds\right], \tag{131}$$
$$\Rightarrow \frac{d}{d\alpha} U(x(\alpha), y) = igA_\mu(x)\frac{dx^\mu}{d\alpha} U(x(\alpha), y), \tag{132}$$
$$\Rightarrow \frac{dx^\mu}{d\alpha}\left(D_\mu U(x(\alpha), y)\right) = 0. \tag{133}$$

Note from the definition of $U(x,y)$ that we have $U(x,y) = 1$ when $x = y$. Thus we have derived a first order differential equation for $U(x,y)$ with boundary conditions.

Applying a gauge transformation to this equation gives

$$\frac{dx^\mu}{d\alpha}\left(D'_\mu U'(x(\alpha), y)\right) = 0. \tag{134}$$

Where D'_μ and U' are D_μ and U after gauge transformation. This differential equation must satisfy the same boundary condition $U'(x,y) = 1$ when $x = y$.

We now show that $V(x)\,U(x,y)\,V^{-1}(y)$ satisfies the same differential equation. Using the fact that the field A_μ transforms via $A_\mu \to VA_\mu V^{-1} + \frac{i}{g}(\partial_\mu V)V^{-1}$ we have:

$$\frac{dx^{\mu}}{d\alpha}\left(D'_{\mu}\left(V\left(x\right)U\left(x\left(\alpha\right),y\right)V^{-1}\left(y\right)\right)\right)$$

$$=\frac{dx^{\mu}}{d\alpha}\left(\frac{\partial}{\partial x^{\mu}}+ig\left(V\left(x\right)A_{\mu}\left(x\right)V^{-1}\left(x\right)+\frac{i}{g}\frac{\partial V\left(x\right)}{\partial x^{\mu}}V^{-1}\left(x\right)\right)\right)V\left(x\right)U\left(x,y\right)V^{-1}\left(y\right) \tag{135}$$

$$=\frac{dx^{\mu}}{d\alpha}\left(\frac{\partial V\left(x\right)}{\partial x^{\mu}}U\left(x,y\right)V^{-1}\left(y\right)+V\left(x\right)\frac{\partial U\left(x,y\right)}{\partial x^{\mu}}V^{-1}\left(y\right)\right) \tag{136}$$

$$+\frac{dx^{\mu}}{d\alpha}\left(igV\left(x\right)A_{\mu}\left(x\right)U\left(x,y\right)V^{-1}\left(y\right)-\frac{\partial V\left(x\right)}{\partial x^{\mu}}U\left(x,y\right)V^{-1}\left(y\right)\right) \tag{137}$$

$$=V\left(x\right)\left[\frac{dx^{\mu}}{d\alpha}\left(\frac{\partial U\left(x,y\right)}{\partial x^{\mu}}+igA_{\mu}\left(x\right)\right)\right]V^{-1}\left(y\right) \tag{138}$$

$$=0 \tag{139}$$

Thus U' and $V\left(x\right)U\left(x,y\right)V^{-1}\left(y\right)$ satisfy the same differential equation. But a first order differential equation with boundary conditions has a unique solution. Thus:

$$U'\left(x,y\right)=V\left(x\right)U\left(x,y\right)V^{-1}\left(y\right), \tag{140}$$

as required.

A.3 Calculus with Grassmann variables

Here we construct the notion of a differential operator acting on a function of Grassmann variables, as well as a definite integral over Grassmann variables. These derivations rely heavily on treating differentiation and integration as operators which map the set of all Grassmann functions to itself. Before we do this we note some properties of Grassmann functions.

Recall that a Grassmann algebra G is defined such that if $\theta_1, \theta_2 \in G$ then:

$$\theta_1\theta_2 \in G \quad \forall\theta_1,\theta_2 \in G, \tag{141}$$

$$\theta_1\theta_2 = -\theta_2\theta_1 \quad \forall\theta_1,\theta_2 \in G, \tag{142}$$

$$0 \in G. \tag{143}$$

Using this we have:

$$\theta_1\theta_2\theta_1 = -\theta_2\theta_1^2, \tag{144}$$

$$\Rightarrow -\theta_1^2\theta_2 = -\theta_2\theta_1^2, \tag{145}$$

$$\Rightarrow \theta_1^2\theta_2 = \theta_2\theta_1^2. \tag{146}$$

But $\theta_1^2 \in G$ by (141) and therefore must satisfy (142), so if θ_1^2 commutes with θ_2 we must have:

$$\theta_1^2 = 0 \ \forall \theta_1 \in G. \tag{147}$$

So powers of Grassmann variables larger than 1 equal zero. In particular if we have $\theta_1, ..., \theta_n$ Grassmann variables, only terms which are linear in these variables can appear. So a function $f(\theta_1, ..., \theta_n)$ of n Grassmann variables must have the form:

$$f(\theta_1, .., \theta_n) = \sum_{m_i} a_{m_i} \theta_1^{m_1} .. \theta_n^{m_n}, \tag{148}$$

$$m_i = \begin{cases} 0. \\ 1. \end{cases} \tag{149}$$

where a_{m_i} is a complex coefficient. In the above sum, we are summing over all possible powers (0 or 1) in the product $\theta_1^{m_1} ... \theta_n^{m_n}$.

A.3.1 Differentiation of Grassmann variables

Consider the differential operator $\frac{\partial}{\partial \theta_i}$. Only terms which are linear in Grassmann variables can appear, so we need only consider how this operator acts on products of Grassmann variables. Firstly they must satisfy the condition:

$$\frac{\partial \theta_j}{\partial \theta_i} = \delta_{ij}, \tag{150}$$

$$\Rightarrow \frac{\partial^2 \theta_j}{\partial \theta_i^2} = 0 \, \forall \theta_i. \tag{151}$$

Furthermore, how these operators act on products is non-trivial, due to the anti-commuting nature of Grassmann variables, i.e.

$$\frac{\partial}{\partial\theta_i}\left(\theta_1..\theta_i..\theta_n\right) = \frac{\partial}{\partial\theta_i}\left(\left(-1\right)^{i-1}\theta_i\theta_1..\theta_{i-1}\theta_{i+1}..\theta_n\right) \tag{152}$$

$$= \left(-1\right)^{i-1}\theta_1..\theta_{i-1}\theta_{i+1}..\theta_n, \tag{153}$$

where have had to commute θ_i to the front of the product to act on it with $\frac{\partial}{\partial\theta_i}$. Since there are $(i-1)$ terms in front of θ_i this gives a factor of $\left(-1\right)^{i-1}$

Finally consider differential operators of the form $\frac{\partial^2}{\partial\theta_i\partial\theta_j}$ where, without loss of generality, $i<j$:

$$\frac{\partial^2}{\partial\theta_i\partial\theta_j}\left(\theta_1..\theta_i..\theta_j..\theta_n\right) = \frac{\partial}{\partial\theta_i}\left(-1\right)^{j-1}\theta_1..\theta_i..\theta_n$$

$$= \left(-1\right)^{j-1}\left(-1\right)^{i-1}\theta_1...\theta_n. \tag{154}$$

Reversing the order of the operators we obtain:

$$\frac{\partial^2}{\partial\theta_j\partial\theta_i}\left(\theta_1..\theta_i..\theta_j..\theta_n\right) = \left(-1\right)^{i-1}\frac{\partial}{\partial\theta_j}\theta_1..\theta_j..\theta_n$$

$$= \left(-1\right)^{i-1}\left(-1\right)^{j-2}\theta_1...\theta_n$$

$$= -\frac{\partial^2}{\partial\theta_i\partial\theta_j}\left(\theta_1..\theta_i..\theta_j..\theta_n\right). \tag{155}$$

Thus second order derivatives of Grassmann variables are anti-symmetric:

$$\frac{\partial^2}{\partial\theta_i\partial\theta_j} = -\frac{\partial^2}{\partial\theta_j\partial\theta_i}. \tag{156}$$

A.3.2 Integration of Grassmann variables

We now construct the notion of a definite integral over Grassmann variables. First we note two conditions that such an integral must satisfy:

$$\int d\theta_i\left(\frac{\partial}{\partial\theta_i}f\left(\theta_1,..,\theta_n\right)\right) = 0, \tag{157}$$

$$\frac{\partial}{\partial\theta_i}\left(\int d\theta_i f\left(\theta_1,...,\theta_n\right)\right) = 0. \tag{158}$$

The first condition comes from the fact that the integral of a derivative is zero in the absence of boundary terms. The second comes from the fact that when θ_i is integrated out, the resulting function is independent of θ_i and so its derivative with respect to θ_i should be zero. We can combine these two conditions into the following:

$$\frac{\partial}{\partial\theta_i}\int d\theta_i = \int d\theta_i \frac{\partial}{\partial\theta_i} = 0. \tag{159}$$

But recall that this is precisely the same condition satisfied by the second order derivative (151). Thus we have:

$$\frac{\partial}{\partial\theta_i} \equiv \int d\theta_i. \tag{160}$$

We end by considering integrals of the form $\int d\theta_1 d\theta_2$, since such integrals appears when integrating over the fermionic fields ψ and $\overline{\psi}$. Using the result above we have:

$$\int d\theta_1 d\theta_2 \ 1 = 0, \tag{161}$$

$$\int d\theta_1 d\theta_2 \ \theta_1 = 0, \tag{162}$$

$$\int d\theta_1 d\theta_2 \ \theta_2 = 0, \tag{163}$$

$$\int d\theta_1 d\theta_2 \ \theta_2\theta_1 = 1. \tag{164}$$

A.4 Continuum limit of the Wilson Gauge Action

We take of the continuum limit, i.e. the limit as $a \to 0$, of the Wilson Gauge action, which is defined as:

$$S_{\mathrm{WG}} = \sum_{\square} S_{\square}, \tag{165}$$

$$S_{\square} = \frac{2N_c}{g^2}\left(1 - \frac{1}{N_c}\mathrm{tr}\left\{U_{n(n+a\hat{\mu})}U_{(n+a\hat{\mu})(n+a\hat{\mu}+a\hat{\nu})}U_{(n+a\hat{\mu}+a\hat{\nu})(n+a\hat{\nu})}U_{(n+a\hat{\nu})n}\right\}\right). \tag{166}$$

Using the identity $U_{nm} = U^{\dagger}_{mn}$ we have:

$$S_{\square} = \frac{2N_c}{g^2}\left(1 - \frac{1}{N_c}\mathrm{tr}\left\{U_{n(n+\mu)}U_{(n+\mu)(n+\mu+\nu)}U_{(n+\mu+\nu)(n+\nu)}U_{(n+\nu)n}\right\}\right)$$
$$= \frac{2N_c}{g^2}\left(1 - \frac{1}{N_c}\mathrm{tr}\left\{U_{n(n+\mu)}U_{(n+\mu)(n+\mu+\nu)}U^{\dagger}_{(n+\nu)(n+\mu+\nu)}U^{\dagger}_{n(n+\nu)}\right\}\right). \tag{167}$$

To take the continuum limit of this we consider the point

$$x = n + \frac{\mu}{2} + \frac{\nu}{2}. \tag{168}$$

When then assume that the gauge fields are smooth enough that we can Taylor expand them about this point x_μ.

Recall the expression for the link element:

$$U_{n(n+\mu)} = \exp\left[igaA_\mu\left(x - \frac{a}{2}\hat{\nu}\right)\right], \tag{169}$$

where we assign A_μ to the midpoint of the link. Consider the product $U_{n(n+\mu)}U_{(n+\mu)(n+\mu+\nu)}$ which appears in the trace. Using (169) we can write this product as:

$$U_{n(n+\mu)}U_{(n+\mu)(n+\mu+\nu)} = \exp\left[igaA_\mu\left(x - \frac{a}{2}\hat{\nu}\right)\right]\exp\left[igaA_\nu\left(x + \frac{a}{2}\hat{\mu}\right)\right]. \tag{170}$$

Taking the product of these exponentials is non-trivial due to the non-abelian nature of the field A_μ. To take this product we make use of the Baker-Campbell-Haussdorff formula:

$$\exp[x]\exp[y] = \exp\left[x + y + \frac{1}{2}[x,y] + ..\right]. \tag{171}$$

The higher order terms in this formula have been neglected since we will be evaluating the exponent of (170) up to order $\mathcal{O}\left(a^2\right)$ since all higher order terms will vanish in the $a \to 0$ limit. Using this we have:

$$U_{n(n+\mu)}U_{(n+\mu)(n+\mu+\nu)} = \exp\left[igaA_\mu\left(x - \frac{a}{2}\hat{\nu}\right) + igaA_\nu\left(x + \frac{a}{2}\hat{\mu}\right) + \frac{1}{2}igaA_\mu\left(x - \frac{a}{2}\hat{\nu}\right), igaA_\nu\left(x + \frac{a}{2}\hat{\mu}\right)\right] \tag{172}$$
$$= \exp\left[iga\left(A_\mu(x) + A_\nu(x)\right) + \frac{iga^2}{2}\partial_\mu A_\nu - \frac{iga^2}{2}\partial_\nu A_\mu - \frac{g^2a^2}{2}\left[A_\mu(x), A_\nu(x)\right] + \mathcal{O}\left(a^3\right)\right] \tag{173}$$
$$= \exp\left[iga\left(A_\mu(x) + A_\nu(x)\right) + \frac{iga^2}{2}F_{\mu\nu} - \frac{g^2a^2}{2}\left[A_\mu(x), A_\nu(x)\right]\right]. \tag{174}$$

Notice that in line (173) we Taylor expanded the field A_μ up to order a about the point x. We then neglected term of order a^3 and higher. Similarly we can derive an expression for the second product appearing in the trace, namely, $U^\dagger_{(n+\nu)(n+\mu+\nu)}U^\dagger_{n(n+\nu)}$, it reads:

$$U^\dagger_{(n+\nu)(n+\mu+\nu)}U^\dagger_{n(n+\nu)} = \exp\left[-iga\left(A_\mu\left(x\right)+A_\nu\left(x\right)\right)+\frac{iga^2}{2}F_{\mu\nu}-\frac{g^2a^2}{2}\left[A_\mu\left(x\right),A_\nu\left(x\right)\right]\right]. \tag{175}$$

Finally, to evaluate the full product, $U_{n(n+\mu)}U_{(n+\mu)(n+\mu+\nu)}U^\dagger_{(n+\nu)(n+\mu+\nu)}U^\dagger_{n(n+\nu)}$, we once again make use of (171). This gives:

$$U_{n(n+\mu)}U_{(n+\mu)(n+\mu+\nu)}U^\dagger_{(n+\nu)(n+\mu+\nu)}U^\dagger_{n(n+\nu)} = \exp\left[iga^2F_{\mu\nu}-g^2a^2\left[A_\mu\left(x\right),A_\nu\left(x\right)\right]+\mathcal{O}\left(a^3\right)\right] \tag{176}$$

$$= \exp\left[iga^2\left(F_{\mu\nu}+ig\left[A_\mu,A_\nu\right]\right)\right] \tag{177}$$

$$= \exp\left[iga^2G_{\mu\nu}\right], \tag{178}$$

where we have, once more, neglected terms of order a^3 and higher. We can now expand this exponential function, expanding up to a^4 gives:

$$U_{n(n+\mu)}U_{(n+\mu)(n+\mu+\nu)}U^\dagger_{(n+\nu)(n+\mu+\nu)}U^\dagger_{n(n+\nu)} = 1+iga^2G_{\mu\nu}-g^2a^4\left(G_{\mu\nu}\right)^2+\mathcal{O}\left(a^6\right). \tag{179}$$

Recall from (166) that the definition of the Wilson gauge action requires us to take the trace of this product. Doing this gives:

$$\mathrm{tr}\left\{U_{n(n+\mu)}U_{(n+\mu)(n+\mu+\nu)}U^\dagger_{(n+\nu)(n+\mu+\nu)}U^\dagger_{n(n+\nu)}\right\} = \mathrm{tr}\left\{1+iga^2G_{\mu\nu}-g^2a^4\left(G_{\mu\nu}\right)^2\right\} \tag{180}$$

$$= N_c-g^2a^4\mathrm{tr}\left(G_{\mu\nu}\right)^2. \tag{181}$$

We finally have an expression for the Wilson gauge action which allows us to easily take the continuum limit:

$$S_{\mathrm{WG}} = \sum_{\square}S_{\square} \tag{182}$$

$$= \sum_x\sum_{\mu,\nu<\mu}\frac{2N_c}{g^2}\left(1-\frac{1}{N_c}\left(N_c-g^2a^4\mathrm{tr}\left(G_{\mu\nu}\right)^2\right)\right) \tag{183}$$

$$= \sum_x a^4G_{\mu\nu}G^{\mu\nu}. \tag{184}$$

We now take the continuum limit, i.e. $a \to 0$. Identifying a^4 as the volume element d^4x, and replacing the sum over all points with an integral yields:

$$S_{\mathrm{WG}} = \sum_x a^4 G_{\mu\nu} G^{\mu\nu} \tag{185}$$

$$\to \int d^4x G_{\mu\nu} G^{\mu\nu} \tag{186}$$

as required.

A.5 Continuum limit of the Wilson Fermion Action

Recall that in Euclidean space, the fermion action is:

$$S_{\mathrm{F}} = \int d^4x \, \overline{\psi} \left(\gamma_E^\mu D_\mu + m\right) \psi. \tag{187}$$

To find a lattice action which converges to this we first show that the expression

$$\frac{1}{2a}\left(U_{n(n+\hat{\mu})}\psi_{n+\hat{\mu}} - U^\dagger_{n(n-\hat{\mu})}\psi_{n-\hat{\mu}}\right) \tag{188}$$

converges to $D_\mu \psi$. Note for $U_{n(n+\hat{\mu})}$ we have:

$$\begin{aligned} U_{n(n+\hat{\mu})} &= \exp\left[igaA_\mu\left(x + \frac{a\hat{\mu}}{2}\right)\right] \\ &= 1 + igaA_\mu\left(x + \frac{a\hat{\mu}}{2}\right) + \mathcal{O}\left(a^2\right). \end{aligned} \tag{189}$$

Plugging this in we have:

$$\frac{1}{2a}\left(U_{n(n+\hat{\mu})}\psi_{n+\hat{\mu}} - U^\dagger_{n(n-\hat{\mu})}\psi_{n-\hat{\mu}}\right) = \frac{1}{2a}\left(\left(1 + igaA_\mu\left(x + \frac{a\hat{\mu}}{2}\right)\right)\psi_{n+\hat{\mu}} - \left(1 - igaA_\mu\left(x - \frac{a\hat{\mu}}{2}\right)\right)\psi_{n-\hat{\mu}}\right) \tag{190}$$

$$= \frac{1}{2a}\left(\psi_{n+\hat{\mu}} - \psi_{n-\hat{\mu}}\right) + \frac{iga}{2a}\left(A_\mu\left(x + \frac{a\hat{\mu}}{2}\right) + A_\mu\left(x - \frac{a\hat{\mu}}{2}\right)\right) \tag{191}$$

$$\to \partial_\mu \psi + igA_\mu \psi \tag{192}$$

$$= D_\mu \psi. \tag{193}$$

Since this converges to $D_\mu\psi$ we can replace $D_\mu\psi$ with this expression when discretizing the fermion action, furthermore we make the replacement $\int d^4x \to a^4\sum_n$. This gives the lattice action:

$$S = a^4 \sum_n \overline{\psi}_n \left(\gamma_E^\mu \left(\frac{1}{2a} \left(U_{n(n+\hat{\mu})} \psi_{n+\hat{\mu}} - U^\dagger_{n(n-\hat{\mu})} \psi_{n-\hat{\mu}} \right) \right) + m\psi_n \right). \quad (194)$$

Wilson proposed adding an additional term to this action which is linear in a[6]. Such a term will vanish in the continuum limit, and so, leaves the physics unchanged. This term is[7]:

$$a\overline{\psi}_n \left(\frac{U_{n(n+\hat{\mu})}\psi_{n+\hat{\mu}} + U^\dagger_{n(n-\hat{\mu})}\psi_{n-\hat{\mu}} - 2\psi_n}{a^2} \right). \quad (195)$$

Thus the full Wilson fermion action is:

$$\begin{aligned} S_{\mathrm{WF}} &= a^4 \sum_n \overline{\psi}_n \left(\gamma_E^\mu \left(\frac{1}{2a} \left(U_{n(n+\hat{\mu})} \psi_{n+\hat{\mu}} - U^\dagger_{n(n-\hat{\mu})} \psi_{n-\hat{\mu}} \right) \right) + m\psi_n \right) \\ &\quad + a\overline{\psi}_n \left(\frac{U_{n(n+\hat{\mu})}\psi_{n+\hat{\mu}} + U^\dagger_{n(n-\hat{\mu})}\psi_{n-\hat{\mu}} - 2\psi_n}{a^2} \right) \quad (196) \\ &= a^4 \sum_n \overline{\psi}_n \left(\left(\frac{1+\gamma_E^\mu}{a} \right) U_{n(n+\hat{\mu})}\psi_{n+\hat{\mu}} + \left(\frac{1-\gamma_E^\mu}{a} \right) U^\dagger_{n(n-\hat{\mu})}\psi_{n-\hat{\mu}} \right) + \left(m - \frac{2}{a} \right) \overline{\psi}_n\psi_n \quad (197) \\ &= \sum_n a^3 \overline{\psi}_n \left((1+\gamma_E^\mu)\, U_{n(n+\hat{\mu})}\psi_{n+\hat{\mu}} + (1-\gamma_E^\mu)\, U^\dagger_{n(n-\hat{\mu})}\psi_{n-\hat{\mu}} \right) + \left(a^4 m - 2a^3 \right) \overline{\psi}_n\psi_n. \quad (198) \end{aligned}$$

Finally, for convenience we rescale the field ψ by a factor of $\sqrt{a^4 m - 2a^3}$. This gives us our final expression:

$$S_{WF} = \sum_n a^3 \overline{\psi}_n \left(\psi_n + \kappa\,(1-\gamma_E^\mu)\, U^\dagger_{n(n-\hat{\mu})}\psi_{n-\hat{\mu}} + \kappa\,(1+\gamma_E^\mu)\, U_{n(n+\hat{\mu})}\psi_{n+\hat{\mu}} \right), \quad (199)$$

where $\kappa = \sqrt{a^4 m - 2a^3}$ is a factor obtained when rescaling our fields.

[6] This term is added to suppress fermion doubling.

[7] To see that this term is proportional to a rather than $\frac{1}{a}$, notice that the term inside the brackets is independent of a since it is just the discretized version of the operator $\nabla_{L,\mu}\nabla_{R,\mu}$ where L and R denote a left and right derivative respectively.

A.6 Integration of the fermionic fields

Consider the fermion action in Euclidean space:

$$S_E = \int d^4x\, L_E \tag{200}$$

$$= \int d^4x \overline{\psi} \left(\gamma_E^\mu D_\mu + m\right) \psi \tag{201}$$

$$= \int d^4x \overline{\psi} M \psi. \tag{202}$$

where M is the square matrix given by $M = \gamma_E^\mu D_\mu + m$. We wish to evaluate the integral:

$$\int D\overline{\psi} D\psi \exp\left[-S_E\right] = \int D\overline{\psi} D\psi \exp\left[-\int d^4x \overline{\psi} M \psi\right]. \tag{203}$$

To do this we consider the eigeanstates ϕ_n with eigenvalues λ_n of M. We can expand ψ and $\overline{\psi}$ in terms of ϕ_n since these eigeanstates form an orthonormal basis:

$$\psi = \sum_n a_n \phi_n, \tag{204}$$

$$\overline{\psi} = \sum_n \overline{a}_n \phi_n^\dagger, \tag{205}$$

$$\int d^4x \phi_n^\dagger \phi_m = \delta_{nm}, \tag{206}$$

where the coefficients a_n are Grassmann variables. Plugging this in we get:

$$\int D\overline{\psi} D\psi \exp\left[-S_E\right] = \int D\overline{\psi} D\psi \exp\left[-\int d^4x \overline{\psi} M \psi\right] \tag{207}$$

$$= \int \prod_n D\overline{a}_n Da_n \exp\left[-\sum_n \left(\overline{a}_n \lambda_n a_n \int d^4x \phi_n^\dagger \phi_n\right)\right] \tag{208}$$

$$= \int \prod_n D\overline{a}_n Da_n \exp\left[-\sum_n \overline{a}_n \lambda_n a_n\right]. \tag{209}$$

But note from (A.3) that

$$\int D\overline{a}Da \exp\left[-\overline{a}\lambda a\right] = \int D\overline{a}Da\ (1+\lambda a\overline{a}) \tag{210}$$

$$= \lambda, \tag{211}$$

$$\Rightarrow \int \prod_n D\overline{a}_n Da_n \exp\left[-\sum_n \overline{a}_n \lambda_n a_n\right] = \prod_n \lambda_n \tag{212}$$

$$= \det(M). \tag{213}$$

A.7 $\det(M)$ is real for $\mu = 0$ and complex for $\mu \neq 0$

In Euclidean space we have the following expression for M:

$$M = \gamma_E^\mu D_\mu + m. \tag{214}$$

Now consider the operator $\gamma^5 M$. First we show that this operator is Hermitian:

$$\begin{aligned}
\left(\gamma^5 M\right)^\dagger &= M^\dagger \gamma^5 \\
&= \left(\gamma^\mu D_\mu + m\right)^\dagger \gamma^5 \\
&= \left(-\gamma^\mu D_\mu + m\right) \gamma^5 \\
&= \gamma^5 \left(\gamma^\mu D_\mu + m\right) \\
&= \gamma^5 M, && (215)\\
\Rightarrow M^\dagger &= \gamma^5 M \gamma^5. && (216)
\end{aligned}$$

Now we take the determinant of both sides to get the desired result:

$$\begin{aligned}
\det\left(M^\star\right) &= \det\left(M^\dagger\right) \\
&= \det\left(\gamma^5 M \gamma^5\right) \\
&= \det(M), && (217)\\
\Rightarrow \det(M) &\in \mathbb{R}. && (218)
\end{aligned}$$

Consider the case when $\mu \neq 0$. Then for $M(\mu)$ we have:

$$M(\mu) = \gamma_E^\mu D_\mu + m + \gamma^0 \mu. \tag{219}$$

Once again me consider the operator $\gamma^5 M(\mu)$ and show that its hermicity is broken for $\mu \neq 0$:

$$\begin{aligned}
\left(\gamma^5 M(\mu)\right)^\dagger &= M^\dagger(\mu)\gamma^5 \\
&= \left(\gamma^\mu D_\mu + m + \gamma^0\mu\right)^\dagger \gamma^5 \\
&= \left(-\gamma^\mu D_\mu + m + \gamma^0\mu\right)\gamma^5 \\
&= \gamma^5\left(\gamma^\mu D_\mu + m - \gamma^0\mu\right) \\
&= \gamma^5 M(-\mu), \qquad (220)\\
\Rightarrow M^\dagger(\mu) &= \gamma^5 M(-\mu)\gamma^5. \qquad (221)
\end{aligned}$$

Taking the determinant of both sides gives:

$$\begin{aligned}
\det\left(M^\star(\mu)\right) &= \det\left(M^\dagger(\mu)\right) \\
&= \det\left(M(-\mu)\right), \qquad (222)\\
\Rightarrow \det\left(M(\mu)\right) &\in \mathbb{C}. \qquad (223)
\end{aligned}$$

A.8 $\det(M(\mu))$ is real in 2 colour QCD

The proof of this result relies on the fact that $SU(2)$ is psuedo-real i.e. the generators of $SU(2)$ in the adjoint representation satisfy the equation:

$$-(T^a)^\star = \sigma_2 T^a \sigma_2^{-1}, \qquad (224)$$

where σ_2 is the second Pauli matrix. We can apply (224) to the field A_μ:

$$\begin{aligned}
\sigma_2 A_\mu \sigma_2^{-1} &= \sigma_2\left(A_\mu^a T^a\right)\sigma_2^{-1} \\
&= -A_\mu^a (T^a)^\star \\
&= -A_\mu^\star. \qquad (225)
\end{aligned}$$

We now consider the operator $U = C\gamma^5\sigma_2$ where C is the charge conjugation operator (i.e. $C\gamma^\mu C^{-1} = -(\gamma^\mu)^T$). Using this we have:

$$\begin{aligned}
UM(\mu)U^{-1} &= \left(C\gamma^5\sigma_2\right)\left(\gamma^\mu\partial_\mu - ig\gamma^\mu A_\mu + m + \gamma^0\mu\right)\sigma_2^{-1}\gamma^5 C^{-1} \qquad (226)\\
&= C\gamma^5\left(\gamma^\mu\partial_\mu - ig\gamma^\mu\left(-A_\mu^\star\right) + m + \gamma^0\mu\right)\gamma^5 C^{-1} \qquad (227)\\
&= C\left(-\gamma^\mu\partial_\mu - ig\gamma^\mu A_\mu^\star + m - \gamma^0\mu\right)C^{-1} \qquad (228)\\
&= (\gamma^\mu)^T\partial_\mu + ig(\gamma^\mu)^T A_\mu^\star + m + \left(\gamma^0\right)^T\mu \qquad (229)\\
&= \left((\gamma^\mu)^\dagger\partial_\mu - ig(\gamma^\mu)^\dagger A_\mu + m + \left(\gamma^0\right)^\dagger\mu\right)^\star \qquad (230)\\
&= \left(\gamma^\mu\partial_\mu - ig\gamma^\mu A_\mu + m + \gamma^0\mu\right)^\star \qquad (231)\\
&= M^\star(\mu). \qquad (232)
\end{aligned}$$

Taking the determinant we have:

$$\det\left(M^{\star}\left(\mu\right)\right) = \det\left(UM\left(\mu\right)U^{-1}\right) = \det\left(M\left(\mu\right)\right), \tag{233}$$

$$\Rightarrow \det\left(M\left(\mu\right)\right) \in \mathbb{R}. \tag{234}$$

A.9 Thermal correlators

Recall that the time evolution of a field ψ is given by the Hamiltonian via the equation

$$\psi\left(t,x\right) = e^{iHt}\psi\left(0,x\right)e^{-iHt}. \tag{235}$$

Writing the expression for $\left\langle \psi\left(t,x\right)\psi\left(0,y\right)\right\rangle_{T}$ explicitly we have:

$$\left\langle \psi\left(t,x\right)\psi\left(0,y\right)\right\rangle_{T} = \frac{1}{Z}\mathrm{tr}\left\{e^{-\beta H}\psi\left(t,x\right)\psi\left(0,y\right)\right\} \tag{236}$$

$$= \frac{1}{Z}\mathrm{tr}\left\{\psi\left(0,y\right)e^{-\beta H}\psi\left(t,x\right)\right\} \tag{237}$$

$$= \frac{1}{Z}\mathrm{tr}\left\{e^{-\beta H}e^{\beta H}\psi\left(0,y\right)e^{-\beta H}\psi\left(t,x\right)\right\} \tag{238}$$

$$= \frac{1}{Z}\mathrm{tr}\left\{e^{-\beta H}\left(e^{iH(-i\beta)}\psi\left(0,y\right)e^{-iH(i\beta)}\right)\psi\left(t,x\right)\right\} \tag{239}$$

$$= \frac{1}{Z}\mathrm{tr}\left\{e^{-\beta H}\psi\left(-i\beta,y\right)\psi\left(t,x\right)\right\} \tag{240}$$

$$= \left\langle \psi\left(-i\beta,y\right)\psi\left(t,x\right)\right\rangle_{T}. \tag{241}$$

where, line (190) we used the cyclic property of the trace and in (193) we time evolved $\psi\left(0,y\right)$ via the Hamiltonian operator.

References

[1] Gert Aarts, Chris Allton, Alessandro Amato, Pietro Giudice, Simon Hands, and Jon-Ivar Skullerud. Electrical conductivity and charge diffusion in thermal qcd from the lattice. *Journal of High Energy Physics*, 2015(2):186, 2015.

[2] N Yu Astrakhantsev, VG Bornyakov, VV Braguta, E-M Ilgenfritz, A Yu Kotov, AV Molochkov, AA Nikolaev, and A Rothkopf. Lattice study of static quark-antiquark interactions in dense quark matter. *arXiv preprint arXiv:1808.06466*, 2018.

[3] Tamer Boz, Seamus Cotter, Leonard Fister, Dhagash Mehta, and Jon-Ivar Skullerud. Phase transitions and gluodynamics in 2-colour matter at high density. *The European Physical Journal A*, 49(7):87, 2013.

[4] Nora Brambilla, S Eidelman, BK Heltsley, R Vogt, GT Bodwin, E Eichten, AD Frawley, AB Meyer, RE Mitchell, V Papadimitriou, et al. Heavy quarkonium: progress, puzzles, and opportunities. *The European Physical Journal C*, 71(2):1534, 2011.

[5] Nora Brambilla, Jacopo Ghiglieri, Antonio Vairo, and Peter Petreczky. Static quark-antiquark pairs at finite temperature. *Physical Review D*, 78(1):014017, 2008.

[6] Nora Brambilla, Antonio Pineda, Joan Soto, and Antonio Vairo. Effective-field theories for heavy quarkonium. *Reviews of Modern Physics*, 77(4):1423, 2005.

[7] Lowell S Brown and William I Weisberger. Remarks on the static potential in quantum chromodynamics. *Physical Review D*, 20(12):3239, 1979.

[8] Yannis Burnier and Alexander Rothkopf. Disentangling the timescales behind the nonperturbative heavy quark potential. *Physical Review D*, 86(5):051503, 2012.

[9] Yannis Burnier and Alexander Rothkopf. Bayesian approach to spectral function reconstruction for euclidean quantum field theories. *Physical review letters*, 111(18):182003, 2013.

[10] Yannis Burnier and Alexander Rothkopf. Hard thermal loop benchmark for the extraction of the nonperturbative q q^{-} potential. *Physical Review D*, 87(11):114019, 2013.

[11] Yannis Burnier and Alexander Rothkopf. A gauge invariant debye mass and the complex heavy-quark potential. *Physics Letters B*, 753:232–236, 2016.

[12] Yannis Burnier and Alexander Rothkopf. Complex heavy-quark potential and debye mass in a gluonic medium from lattice qcd. *Physical Review D*, 95(5):054511, 2017.

[13] Seamus Cotter, Pietro Giudice, Simon Hands, and Jon-Ivar Skullerud. Towards the phase diagram of dense two-color matter. *Physical Review D*, 87(3):034507, 2013.

[14] Simon Duane, Anthony D Kennedy, Brian J Pendleton, and Duncan Roweth. Hybrid monte carlo. *Physics letters B*, 195(2):216–222, 1987.

[15] John M Hammersley and DC Handscomb. Percolation processes. In *Monte Carlo Methods*, pages 134–141. Springer, 1964.

[16] Simon Hands, Seyong Kim, and J-I Skullerud. Deconfinement in dense two-color qcd. *The European Physical Journal C-Particles and Fields*, 48(1):193–206, 2006.

[17] Frithjof Karsch, MT Mehr, and Helmut Satz. Color screening and deconfinement for bound states of heavy quarks. *Zeitschrift für Physik C Particles and Fields*, 37(4):617–622, 1988.

[18] Mikko Laine, Owe Philipsen, Marcus Tassler, and Paul Romatschke. Real-time static potential in hot qcd. *Journal of High Energy Physics*, 2007(03):054, 2007.

[19] T Matsui and Helmut Satz. J/ψ suppression by quark-gluon plasma formation. *Physics Letters B*, 178(4):416–422, 1986.

[20] Keith A Olive, Particle Data Group, et al. Review of particle physics. *Chinese Physics C*, 38(9):090001, 2014.

[21] Peter Petreczky, Alexander Rothkopf, and Johannes Weber. Realistic in-medium heavy-quark potential from high statistics lattice qcd simulations. *arXiv preprint arXiv:1810.02230*, 2018.

[22] William H Press, Saul A Teukolsky, William T Vetterling, and Brian P Flannery. *Numerical recipes 3rd edition: The art of scientific computing*. Cambridge university press, 2007.

[23] Alexander Rothkopf, Tetsuo Hatsuda, and Shoichi Sasaki. Complex heavy-quark potential at finite temperature from lattice qcd. *Physical review letters*, 108(16):162001, 2012.

[24] Lata Thakur, Najmul Haque, Uttam Kakade, and Binoy Krishna Patra. Dissociation of quarkonium in an anisotropic hot qcd medium. *Physical Review D*, 88(5):054022, 2013.